Repository Istituzionale dei Prodotti della Ricerca del Politecnico di Bari

The effects of incident electric fields on counterflow diffusion flames

This is a post print of the following article

Original Citation:
The effects of incident electric fields on counterflow diffusion flames / Di Renzo, M.; Urzay, J.; De Palma, P.; de Tullio, M. D.; Pascazio, G.. - In: COMBUSTION AND FLAME. - ISSN 0010-2180. - STAMPA. - 193:(2018), pp. 177-191. [10.1016/j.combustflame.2018.03.001]

Availability:
This version is available at http://hdl.handle.net/11589/128798 since: 2022-06-05

Published version
DOI:10.1016/j.combustflame.2018.03.001

Publisher:

Terms of use:

(Article begins on next page)

12 October 2024

Version of Record: https://www.sciencedirect.com/science/article/pii/S0010218018301019
Manuscript_9ac43e0f3a2406c8e5d170749c56e4b7

The effects of incident electric fields on counterflow diffusion flames

Mario Di Renzo[a,b], Javier Urzay[a,*], Pietro De Palma[b], Marco D. de Tullio[b], Giuseppe Pascazio[b]

[a] *Center for Turbulence Research, Stanford University, Stanford, CA 94305-3024, United States*
[b] *Dipartimento di Meccanica, Matematica e Management & Centro di Eccellenza in Meccanica Computazionale, Politecnico di Bari, Bari 70125, Italy*

Abstract

Numerical simulations of counterflow laminar diffusion flames impinged by sub-breakdown DC electric fields are performed in this work using multi-component transport and a detailed chemical mechanism for methane-air combustion that includes elementary steps for the conversion of six electrically charged species. The electric field is induced by two electrodes located on the oxidizer and fuel sides and arranged parallel to the mixing layer in a configuration resembling the one recently studied experimentally by Park *et al.* [1], which unveiled significant electric-field effects on the aerodynamics. In these simulations, the electric drift of the charged species leads to a bi-directional ionic wind that is axially directed toward both injectors. The major components of the ionic winds are the H_3O^+ and $O_2{}^-$ ions, which are steered by the electric field into the fuel and oxidizer streams, respectively. At sufficiently high electric fields of the same order as a few kilovolts per centimeter, the ionic wind intricately couples with the aerodynamic field of neutral molecules flowing into the burner, in a manner that ultimately leads to non-negligible disturbances of the velocity field. The overall effect of these interactions consists of a decrease in the local strain rate and in the stoichiometric scalar dissipation rate, which increases the burning rate of the diffusion flame. The functional form of the scalar dissipation rate depends on the applied electric field, which may have consequences for future subgrid-scale modeling for these processes. In contrast to electrified one-dimensional premixed flames, here the current ceases to vary monotonically with the voltage as a result of the coupling with the aerodynamic field. Comparisons between the present numerical simulations and the experiments performed by Park *et al.* [1] are made that indicate qualitative agreement. Quantitative disagreements related to the saturation intensities and to the strength of the electric disturbances of the velocity field are discussed, and possible sources of these discrepancies are identified.

Keywords: Diffusion flames, Sub-breakdown electric-fields, Chemi-ionization, Electric drift.

1. Introduction

The impingement of electric fields on flames is known to have potential for mitigating combustion instabilities, enhancing flame propagation, and decreasing pollutant emissions [2]. Many different technologies have been proposed to accomplish this objective, but the requirements of low complexity and low power consumption have proven to be very stringent constraints. This method takes advantage of the charged species produced by chemi-ionization kinetics in the flame, thereby generating non-electroneutral regions in the flow field. In particular, the imposed electric field steers the charged species, which exchange momentum with the rest of the gas, thereby changing the flow around the flame and creating an ionic wind whereby anions and cations flow towards the corresponding electrodes. The electric field can shift the flame position and, depending on the configuration and operating parameters, may stabilize combustion while reducing the emission of pollutants.

The effects of electric fields on flames have been observed experimentally in a number of studies. Those experiments have provided detailed analyses of ionic chemistry of hydrocarbon flames [3], laminar premixed-flame speed augmentation by electric fields [4], electric extinction of liquid-pool fires and jet diffusion flames [5], electrically induced instabilities in premixed flames [6], and variations of lift-off heights jet diffusion flames with electric fields [7, 8]. Similarly, reduction in pollutant emissions by using electric fields have been demonstrated for high-power combustors of industrial relevance [9]. Furthermore, active control of small-scale electrified diffusion flames has been performed in earlier experimental works by integrating the burner in an electric circuit to obtain a desired flame response [10]. However, experimental studies tend to be limited to the qualitative characterization of the macroscale dynamics of the flame because of outstanding challenges associated with measuring the distribution of charged species and the hydrodynamic flow field. Numer-

*Corresponding author
Email addresses: mario.direnzo@poliba.it (Mario Di Renzo), jurzay@stanford.edu (Javier Urzay), pietro.depalma@poliba.it (Pietro De Palma), marcodonato.detullio@poliba.it (Marco D. de Tullio), giuseppe.pascazio@poliba.it (Giuseppe Pascazio)

© 2018 published by Elsevier. This manuscript is made available under the Elsevier user license
https://www.elsevier.com/open-access/userlicense/1.0/

ical simulations can palliate these shortcomings and may serve as a complementary tool to understand the flame response to an applied voltage, as shown in this study.

Counterflow laminar diffusion flames represent a cornerstone in subgrid-scale models for nonpremixed turbulent combustion [11, 12]. However, their interactions with electric fields have been the focus of only a very few studies to date. From the computational standpoint, and in contrast to premixed combustion, the effects of electric fields on counterflow diffusion flames have generally received much less attention, although progress has been recently made in simplified models for their interactions with axial electric fields [13]. The early experimental work of Dayal and Pandya [14, 15] employed an electric field generated by two electrodes surrounding each orifice exit of the two opposing nozzles, and showed that the electric interaction shifted an ethyl-alcohol/oxygen diffusion-flame position by ∼5-6% toward the oxidizer side and increased the flame temperature by about 60 K from the nominal unelectrified values. The results were interpreted on the basis of a prevailing chemical effect induced by the electric field on the flame, in that free electrons, produced by the flame and energized by the electric field, enabled dissociation reactions that would have been impossible otherwise, thereby producing oxygen and hydrogen radicals that imbalanced the unelectrified flame structure.

More recently, Park *et al.* [1] studied a similar experimental configuration based on an electrified nonpremixed counterflow burner and included Particle Image Velocimetry (PIV) visualizations of the flow, which is a technique that has been early recognized as challenging to deploy in electrified flames due to potential self-charging of the tracers (e.g., see discussion in Ch. 7 in Ref. [2]). They used two mesh electrodes, which produced an electric field aligned with the axis of the burner that traversed the diffusion flame. The results included electric intensity/voltage curves revealing differences with respect to previously reported electric responses of premixed flames, such as the emergence of an overcurrent at intermediate voltages. Additionally, the PIV measurements suggested that the dominant electric effect pertained to the momentum coupling with the neutral particles in the form an ionic wind, which appeared to vastly modify the flow structure to the extent that an extra stagnation plane induced by the electric interactions was observed in some cases. The numerical simulation of the experimental configuration employed by Park *et al.* [1] is the focus of the present study with the goal of elucidating the nature of these flow modifications.

Numerical simulations involving electric-field effects on combustion, subject to detailed chemistry and complex transport, are scarce in the literature and have been mostly limited to one-dimensional (1D) premixed flames[1] [17–22]. In these, the electric force induced by the motion of ions solely acts to readjust the hydrodynamic pressure gradient to satisfy mass conservation. Other problems such as two-dimensional laminar jet flames, where the interactions with the underlying flow field are more complex, have been simulated using skeletal mechanisms [23–25] and flamelet-based models to reduce the computational cost of resolving the reacting layers [26–28]. In most cases, numerical predictions tend to disagree with experimental measurements of electric intensities and charged-species profiles by factors of 2-3, indicating the relatively early stage at which the predictive capabilities in this research discipline are to date.

A number of important barriers, which are clearly manifested also in the present study, hinder the development of theoretical and computational studies of electrified flames. These are related to: (a) the multi-scale nature of the electric/aerothermochemical coupling phenomena, including the existence of a large disparity in time scales of the motion of electrons and neutrals; (b) the complexities associated with the description of the molecular transport of charged species; and (c) the absence of accurate descriptions of ionic chemistry and the overreliance of ionic chemical pathways on the prediction of sub-ppm concentrations of radical precursors.

Each of the barriers outlined above has a corresponding effect on the calculations. Firstly, the wide range of time scales typically leads to an exceedingly high computational cost, particularly in configurations such as the one treated here where the fluid mechanics of the bulk gas plays an important role. Specifically, the chemical kinetics of charged species and the motion of the electrons occur in characteristic time scales that are much shorter than those of convection and diffusion of the bulk gas, thereby causing severe numerical stiffness in the integration of the conservation equations. In the present investigation, a pseudo-time stepping algorithm is developed for a fast approach to a steady solution. Secondly, the molecular transport of charged species requires consideration of electric drift velocities, whose intensities are characterized by electric mobility coefficients that remain largely uncertain in the available literature and therefore lead to potentially different results. The present study employs values of the electron mobility recently updated by Bisetti and El Morsli [18] albeit for planar premixed flames, since studies related to this quantity are even more scarce for counterflow diffusion flames. Lastly, the ionization chemistry of electrified flames relies on the correct prediction of minor neutral intermediates and on the accurate representation of reaction rates for the chemical conversion of charged species. The former requires appropriate mechanisms for the neutrals that can predict minute quantities of radicals such as CH and O, which, in the methane flames addressed here, are believed to be responsible for initiating the ionic radical chains. This is typically attempted by using detailed mechanisms such as the GRIMech 3.0 [29] employed in this study, although it appears to be insufficient as suggested

[1] A recent publication by Belhi et al. [16], which addresses numerically a nonpremixed counterflow configuration similar to the one presented in this study, was brought to the attention of the authors during the revision of this manuscript.

by the results presented below. The detailed mechanism for the neutrals requires coupling with a submechanism for ionized species, such as the relatively complex one provided by Belhi *et al.* [27] for lifted jet diffusion flames that is used in the present work.

In this investigation, numerical simulation results are presented for electric-field interactions with counterflow laminar diffusion flames in the configuration depicted in Fig. 1, which is similar to that studied experimentally by Park *et al.* [1] and is described later in the text in Sec. 2. The involved velocities are much smaller than the speed of sound and warrant moderately large Reynolds numbers within the laminar regime, in such a way that the flow remains axisymmetric and mostly steady with some exceptions in particular cases which are outlined below. The analytical formulation of the problem includes a two-way coupled system of conservation equations describing the aerothermochemical and electric fields, multi-component transport coefficients for the involved species, and a detailed chemical mechanism for $CH_4/O_2/N_2$ combustion that accounts for ionic chemistry, as mentioned above. The simulations focus on a set of operating parameters involving a wide range of electric voltages and two different injection mixture compositions. The results include comparisons against experimental velocity fields, quantitative descriptions of the electric effects on the diffusion-flame structure, translations of the results into mixture-fraction space to assess electric effects on the scalar dissipation rate, and an analysis of the impact of the incident electric field on PIV-derived velocity measurements.

The remainder of this paper is structured as follows. The computational set-up and the operating parameters of the counterflow burner are described in Sec. 2. The simulation results are analyzed in Sec. 3. Concluding remarks are given in Sec. 4. Two auxiliary sections are included in the Supplementary Material. Section S1 of the Supplementary Material provides the conservation equations, a brief outline of the chemical mechanism, and descriptions of the transport coefficients and the numerical methods employed to integrate the equations. Section S2 of the Supplementary Material focuses on 1D numerical simulations of electrified premixed flames, which serve to compare the results of the present computational framework with the simulations and experiments in Speelman *et al.* [30] and with 1D solutions of that same problem obtained using Flamemaster [31].

2. Computational set-up

In this section, descriptions of the the computational set-up and burner geometry are outlined, along with the operation parameters and boundary conditions. The reader is referred to Sec. S1 of the Supplementary Material for further details about the analytical and numerical formulations of the problem, including the associated mathematical notation.

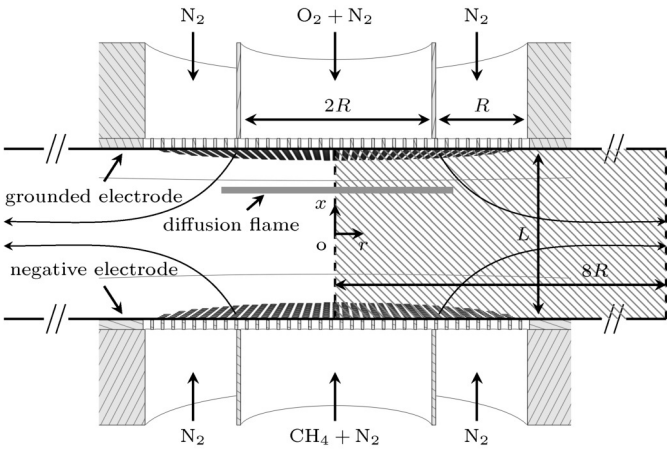

Figure 1: Sketch of the burner geometry and computational set-up (not to scale). The computational domain is denoted by the hatched region, while the two electrodes are represented by the horizontal thick solid lines. The axysimmetric coordinate system $\{x, r\}$ is placed at mid distance between the two orifice exits.

The nonpremixed counterflow burner considered here operates at atmospheric pressure and consists of two opposite cylindrical nozzles of diameter $2R = 1\,\text{cm}$ separated by a distance $L = 1\,\text{cm}$, as depicted in Fig. 1. The computations presented in this study utilize the same geometry and operation parameters as the experiments of Park *et al.* [1]. The conservation equations are discretized on an axisymmetric $\{r, x\}$ domain given by $0 \leq r \leq 8R$ and $-L/2 \leq x \leq +L/2$. The grid is Cartesian and uniform with $N_r \times N_x = 512 \times 256$ points in the radial and axial directions, respectively, which were observed to be effective in resolving the reaction layers. The resulting grid spacings are $\Delta x = L/N_x = 39\,\mu\text{m}$ and $\Delta r = 8R/N_r = 78\,\mu\text{m}$.

The upper ($x = +L/2$) and lower ($x = -L/2$) nozzles inject, respectively, O_2/N_2 and CH_4/N_2 mixtures whose relative compositions can be varied to study the effect of shifting the flame position in composition and physical spaces. In particular, two sets of mixtures are addressed in this study. The first set consists of a 27.4% O_2 / N_2 (on a molar basis) oxidizer mixture flowing against a pure CH_4 fuel stream, which renders a stoichiometric mixture fraction $Z_{st} = 0.07$. Conversely, the second set is based on a fuel-leaner flow whereby a 52.7% O_2 / N_2 oxidizer mixture is employed along with a 22.2% CH_4 / N_2 diluted fuel mixture, which gives $Z_{st} = 0.50$, in such a way that, relative to the first set of conditions, the diffusion flame is shifted toward the fuel injector and becomes comparatively more centered in the burner because of the corresponding spatial variation of the stoichiometric conditions. In both cases, the gases are injected at temperature $T = 300\,\text{K}$ with an axial velocity $U = 20\,\text{cm/s}$, thereby producing a characteristic strain rate $A \sim 2U/L = 40\,\text{s}^{-1}$. The associated Reynolds number is $\text{Re}_L = AL^2/\nu_0 \sim 252$ in both cases, where ν_0 is the kinematic viscosity of the oxidizer stream which has mostly the same value in both

cases. The moderate value of Re_L in principle warrants a mostly laminar steady flow in the burner. Near the stagnation plane created by the two opposing streams, a convective-diffusive mixing layer of characteristic thickness $\delta_m/L = \mathrm{Re}_L^{-1/2} = 0.063$ is formed, within which combustion chemical reactions take place leading to a diffusion flame that has a mostly flat shape near the axis. This mixing layer is resolved by $\delta_m/\Delta x \sim 16$ grid points across. It should be noted that this estimate for δ_m is based on ν_0 and therefore does not account for temperature-dependent effects on the kinematic viscosity, which tend to thicken the mixing layer as shown below.

In the experiments, the nozzles are mounted downstream of convergent sections that reaccelerate the flow and decrease the thickness of the boundary layers at the injection planes. As a result, in the computations, the inflow profiles of axial velocity are assumed to be uniform. Cross-sectional uniformity at injection is also assumed for the temperature and composition fields there. Symmetry conditions are used along the burner axis $r = 0$, whereas standard convective outflow conditions are employed at the outlet plane $r = 8R$.

The fuel and oxidizer nozzles are placed concentrically inside two other cylindrical nozzles of diameter $4R = 2\,\mathrm{cm}$, which inject a nitrogen sheath that stabilizes the mixing layer and prevents chemical reactions with ambient air. The velocity and temperature of the N_2 injected in the sheath is the same as those of the streams flowing out of the main nozzles, with uniform profiles being assumed for all quantities.

A constant (DC) voltage difference $\Delta\Phi_0$ is applied between a grounded anode at $x = +L/2$ and a cathode at $x = -L/2$. To incorporate the electrodes in a parallel arrangement to the diffusion flame, the experiments featured two perforated metallic plates of diameter $8.0\,\mathrm{cm}$ that are positioned at the injection plane of the nozzles. The plates have a high density of holes $n_h = 79\,\mathrm{cm}^{-2}$ and a small diameter per hole $d_h = 0.8\,\mathrm{mm}$. In the simulations, the electrodes are assumed to be perfectly permeable, in that the injected gas flows through them without pressure loss and in the absence of wake effects due to the moderate values of the hole-based Reynolds numbers involved, $\mathrm{Re}_h = 4U/(\pi n_h d_h \nu_0) \sim 26$. Additionally, the two annular portions of the electrodes between the edge of the N_2-sheath injector and the outlet of the computational domain (i.e., $R < r \leq 8R$ at $x = \pm L/2$) are treated, for simplicity, as adiabatic non-slip walls.

The electrode on the fuel side is set to a negative electric potential whose magnitude ranges from 0 to $-2.4\,\mathrm{kV}$ depending on the case considered. This results in a sub-breakdown axial electric field primarily directed from the oxidizer to the fuel side. Correspondingly, the Poisson equation for the electric potential Φ [see Eq. (S1.7) in the Supplementary Material] is integrated subject to Dirichlet boundary conditions at the electrodes along with zero-gradient conditions on all other boundaries.

The boundary conditions for the ionized species are imposed as follows. If the charge of the ionized species is such that they are electrostatically attracted to the electrode, a zero normal-gradient condition is imposed there on the corresponding mass fraction Y_i in order to avoid molecular diffusion of that component into the electrode. In this way, only the electrically-induced drift velocity $\mathbf{V}_i$ is active on the electrode surface, which is associated with the ion current entering the electrode. Conversely, if electrostatic repulsion prevails on the electrode surface for a given component, its mass fraction is set to zero there to prevent any unrealistic flux of opposite-sign ions released by the electrode.

The transfer of momentum between charged and neutral particles is represented by the electric force $\mathbf{f_{el}}$ in the momentum equation (S1.2). This interaction, which, as shown in Sec. 3, primarily occurs outside the mixing layer in the inviscid region along distances of order L, is typically referred to as ionic wind. It represents a two-way coupled effect that can locally modify the flow field of the neutral gas and is quantified by the dimensionless coupling parameter

$$\Xi = (\Delta\Phi_0)^2 \epsilon_0 / (2\rho_0 U^2 L^2) \tag{1}$$

corresponding to the ratio of the characteristic electric force $\rho_{q0} E_0$ to the characteristic convective acceleration $\rho_0 A U$ in (S1.2), with ρ_0 being the gas density in the fuel stream. In Eq. (1), use of the electrostatic scaling of the electric field $E_0 \sim |\Delta\Phi_0|/L$ and of the total charge density $\rho_{q0} \sim |\Delta\Phi_0|\epsilon_0/L^2$ from Eqs. (S1.6)-(S1.7) have been made. In these simulations, Ξ is a small parameter at small voltage differences (i.e., $\Xi \sim 0.2$ at $|\Delta\Phi_0| = 0.5\,\mathrm{kV}$), it increases with the applied voltage, and becomes an order-unity parameter at the upper end of the range of voltages considered here (i.e., $\Xi \sim 3.7$ at $|\Delta\Phi_0| = 2.0\,\mathrm{kV}$, and $\Xi \sim 5.4$ at $|\Delta\Phi_0| = 2.4\,\mathrm{kV}$), thereby highlighting the relevance of the ionic winds in altering the flow field in the selected regimes.

The initial conditions for the simulations correspond to the solution profiles of the aerothermochemical variables obtained for the unlectrified case $\Delta\Phi_0 = 0\,\mathrm{kV}$. The convergence of the simulations to the steady solution, as detailed in Sec. S1.4 of the Supplementary Material, is monitored using the L-infinity norm of a residual vector composed of the pseudo-time derivatives of the temperature, velocity components and species mass fractions, normalized with their maximum values based on the pseudo-time increment. Using this computational framework, each of the 9 different computational cases analyzed below in Sec. 3 involves approximately 70,000 CPU hrs using 128 cores.

3. Numerical Results

This section focuses on the results obtained from numerical integrations of the conservation equations described in Sec. S1.1 of the Supplementary Material in the computational set-up described above. The results include analyses

of the electric intensity/voltage curves as well as characterizations of the influences of the electric field on the velocity field and on the distribution of charged species.

3.1. Electric characteristics of the diffusion flame

Combustion chemical reactions in the diffusion flame alter significantly the linear distribution of electric potential between the electrodes that is encountered in non-reacting conditions, as shown in Fig. 2. In particular, at low voltages compared to a saturation voltage introduced below, the diffusion flame resembles a Faraday cage that blocks the external electric field by the shielding action of abundant electric charges steered outwardly from the reaction region.

The flame-induced screening of the electric field is quantitatively shown by the flattened electric-potential distributions corresponding to $\Delta\Phi_0 = -0.5\,\mathrm{kV}$ and $-1.0\,\mathrm{kV}$ in Fig. 2, and occurs independently of the levels of fuel dilution considered here. In this low-voltage regime, the charges are produced at a plentiful rate by the ionic chemical pathways described in Sec. S1.2 of the Supplementary Material in comparison with their slower drift rate of removal by the electric field from the reaction layers. As a result, the charges become spatially segregated along high-concentration layers surrounding a central zone of much smaller charge where the chemical reactions responsible for producing charged species are important. As shown below in Sec. 3.2, in this plateau the mixture partially conserves the quasi-electroneutrality that characterized the unelectrified case. The two peaks of charge density lead to a dipole of opposite polarity to the external field, as shown in Fig. 3, in a way that makes the diffusion flame to behave as a quasi-perfect conductor with nearly-zero electric field inside. These considerations resemble the mechanism of charge redistribution observed in electrified 1D premixed flames [32].

The configuration with undiluted fuel $Z_{st} = 0.07$ yields stoichiometric conditions closer to the oxidizer injector and, therefore, creates a diffusion flame that acquires an equilibrium potential closer to that of the anode, as observed in Fig. 2a. In contrast, Fig. 2b indicates that intermediate values of the electric potential are attained at the diffusion-flame location when fuel dilution is employed, since the latter displaces stoichiometry toward the fuel orifice. In both cases, a small peak of positive charge is observed in the reacting region in the $-0.5\,\mathrm{kV}$ case, which is caused by a small local excess of the concentration of hydronium (H_3O^+), namely the major positive ion. The distributions of charged species are analyzed later in Sec. 3.2.

As the absolute value of the applied voltage is increased, the magnitude of the positive and negative peaks of the charge density increases and their separation distance decreases. This behavior, however, is non-monotonic with the voltage, as observed in Fig. 3. Specifically, as $|\Delta\Phi_0|$ is increased above 1 kV, the electric field is increasingly less shielded by the charges, which tend to become spatially reorganized more uniformly across the burner, as evidenced

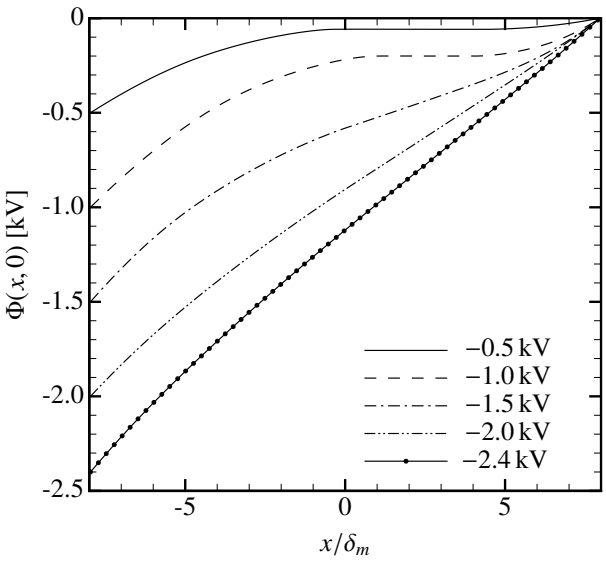

(a)

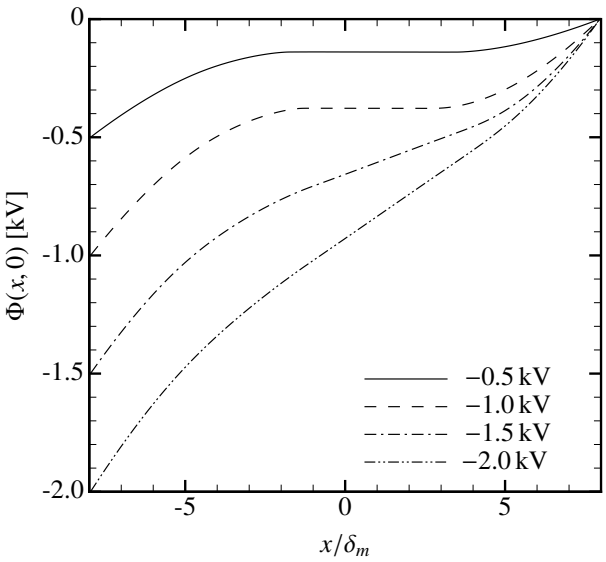

(b)

Figure 2: Dimensional electric potential profiles along the axis of the burner for (a) $Z_{st} = 0.07$ and (b) $Z_{st} = 0.50$.

by the broader and shallower distributions of the charge density shown in Fig. 3. This results in an increasingly linear distribution of electric potential engendering an electric field that pierces into the diffusion flame and eventually reaches values closer to the non-reacting uniform distribution at the largest voltage differences sampled here. Under these conditions, the characteristic production rates of heavy ions are slower than the rates of removal of these by the electric drift term in the diffusion velocity (S1.4). Similarly to the low-voltage case, a plateau of nearly-zero charge is also observed in the electric-charge distribution, although here the rapid electric drift suppresses the charge

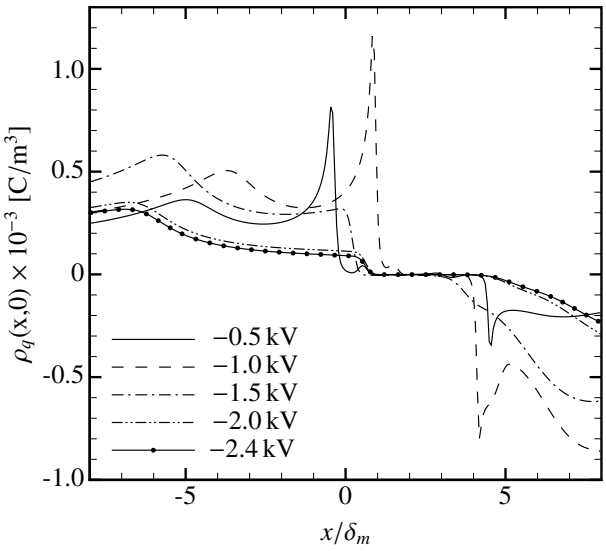

(a)

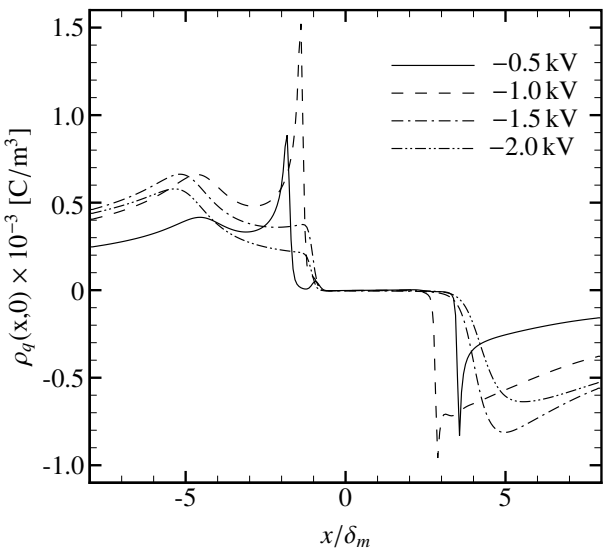

(b)

Figure 3: Dimensional charge density profiles along the axis of the burner for (a) $Z_{st} = 0.07$ and (b) $Z_{st} = 0.50$.

peaks observed at smaller voltages.

The aforementioned changes in the distributions of the electric field and charge density, observed as the applied voltage increases, are closely related to the occurrence of a saturation in the rate of production of charges in the diffusion flame, which intrinsically limits the current density across the burner as follows. In the absence of combustion chemical reactions, the burner behaves as an open circuit when DC voltage is applied to the electrodes. In contrast, the presence of electric charges generated by chemical reactions in the diffusion flame produces a non-zero electric current across the burner, which is predominantly directed downwards along the axial coordinate x and depends on the voltage difference $\Delta\Phi_0$. In particular, Fig. 4 provides the voltage dependence of the electric intensity leaving the top (anode) electrode at $x = L/2$, namely

$$I = \int_0^\infty 2\pi r \sum_{i=1}^{N_s} \rho_{q,i}(u_x + V_{i,x})dr. \tag{2}$$

In the figure, I is divided by the flame area πR_f^2, in a similar way as is reported in the experiments by Park *et al.* [1], with N_s being the number of species, and u_x, $V_{i,x}$ and $\rho_{q,i}$ being the radial distributions of the axial flow velocity, axial diffusion velocities and charge densities, respectively, as prescribed by Eqs. (S1.4) and (S1.8). Specifically, Park *et al.* [1] measured the current between the two electrodes and divided it by an estimated flame area πR_f^2, with R_f a radius determined by the flame luminosity. The corresponding experimental intensity values, which were reported only for the diluted case $Z_{st} = 0.5$, are reproduced here in Fig. 4b. Conversely, in these simulations, R_f is determined by the radial extent of the distribution of the mass fraction of CH (i.e., $r \leq R_f$ where $Y_{\mathrm{CH}} \geq 10^{-9}$), since the chemical mechanism utilized here does not include any of the radiation-emitting species such as OH* or CH*. The resulting flame radius is of order 12 mm and 9 mm for the cases $Z_{st} = 0.50$ and $Z_{st} = 0.07$, respectively, and remains mostly independent of the applied voltage. Since the system is in steady state, the time variations of the total charge in the burner volume are zero. Consequently, charge conservation requires the flux of current density to be the same on each electrode, thereby leading to equal intensities there.

The voltage dependence of the intensity provided by Eq. (2) has a qualitative structure that in principle does not depend on the dilution for the injection conditions analyzed here. In both cases, the intensity increases monotonically for small voltages in a sub-saturated regime (zone A in Fig. 4a), in which the incident electric field is screened by a shield of charges, which are produced abundantly and surround the diffusion flame, as described above and shown in Figs. 2 and 3. The intensity reaches a saturation value near the upper limit of the voltage interval studied here (i.e., at $|\Delta\Phi_0| \sim 2.0$ kV; zone C in Fig. 4a), where the incident electric field supersedes recombination in removing ions, thereby limiting the current by the rate of ionization. A third or overcurrent regime at intermediate voltages (zone B in Fig. 4a), where a peak in intensity occurs, is observed in the experiments for the configuration with $Z_{st} = 0.50$ and numerically in the $Z_{st} = 0.07$ case. In the simulations of the $Z_{st} = 0.50$ case, this overcurrent appears to be absent, which is most likely due to undersampling along the voltage axis.

The overcurrent regime is not typically observed in 1D premixed flames [2, 4, 19, 30, 32] (see also Fig. S2.2 in the Supplementary Material). There, the baseline profiles of the radicals starting the ionic chemistry chain remain mostly unaffected by the electric field. As a result, the

electric current increases monotonically with the applied voltage up to a saturation voltage beyond which it plateaus and where the finite rate of production of charged species becomes the limiting process. In those saturation conditions, and despite the large electric fields, the electric drift flux remains limited by the rate of production of charged species. In contradistinction, as described later in Sec. 3.4, in the present problem the profiles of the radicals starting the ionic chemistry, along with the rates of production of ionized species, are all closely coupled with the strain-rate field. Since the latter is sensitive to the incident electric field, the dependence of the ion-current intensity on the applied voltage does not have to be necessarily monotonic. In this particular case, the presence of the overcurrent is the result of a drop in the limiting current as saturation conditions are approached (i.e., $-2.0\,\mathrm{kV}$) due to the decrease in the scalar dissipation rate, which leads to overall faster chemistry and correspondingly smaller concentrations of charged species.

The comparison between experimental and numerical values of the intensity for the $Z_{st} = 0.5$ case in Fig. 4b reveals some important limitations of the formulation described above. Although the sub-saturated and saturated regimes are present in both experiments and simulations, the simulations tend to overpredict the intensity approximately by a factor of 2.5 with respect to the experimental values, including the saturation range, where the current only depends on the charge-production modeling capability of reaction $\mathrm{CH} + \mathrm{O} \longrightarrow \mathrm{CHO}^+ + \mathrm{e}^-$ (see Sec. S1.2 of the Supplementary Material for descriptions of relevant chemical-kinetic steps involved in the formulation of this problem). Related discussions about similar discrepancies, albeit for premixed flames, are available in Ref. [32]. A similar offset with respect to the experimental measurements carried out by Speelman *et al.* [30] is also observed in the auxiliary simulations of the premixed burner-stabilized premixed flame provided in the Sec. S2 of the Supplementary Material. The magnitude of these mismatches in saturation currents are standard in the general literature of premixed flames and jet flames under electric fields [19, 25, 30], and suggests that the chemical mechanism discussed in Sec. S1.2 of the Supplementary Material also underperforms in configurations involving electrified counterflow diffusion flames. The root cause of this shortcoming resides in the coupling between neutral and ionic chemistries, including inaccuracies in the prediction of CH and O radicals generated from neutral production pathways, and in the large uncertainties associated with the rates of the chemical steps participating in the ionized radical chains. Potential improvements to this framework could include the utilization of extended chemical mechanisms [22, 33, 34] or case-specific optimizations of ionization rates in the submechanism for the charged species [30], although these are aspects that will be subject of future research.

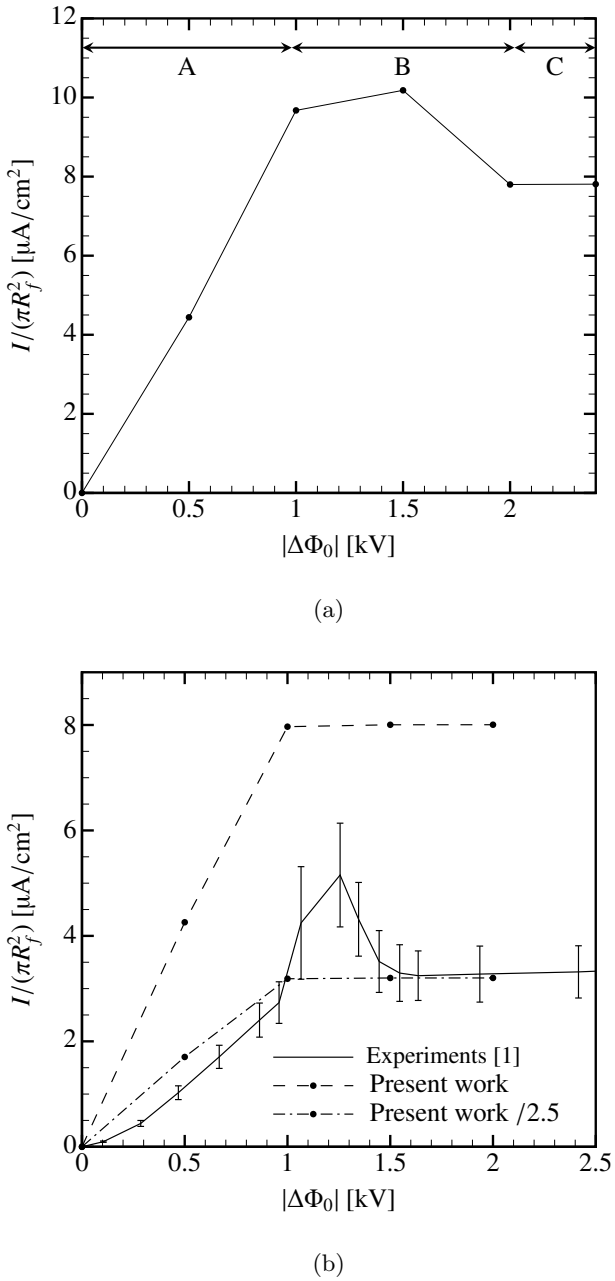

Figure 4: Intensity per unit flame area measured at the top electrode as a function of the voltage difference $|\Delta\Phi_0|$ for (a) $Z_{st} = 0.07$ and (b) $Z_{st} = 0.50$. In panel (b), the experimental data and the associated uncertainty bars are based on Ref. [1].

3.2. Effects of the incident electric field on the diffusion-flame structure

The general structure of non-electrified, methane counterflow diffusion flames has been extensively studied in the past [11, 35] and remains qualitatively unaltered in the range of voltages studied here. The most relevant effect of the incident electric field, however, is to alter significantly the distribution of minor charged intermediates, whose momentum exchange with the neutral molecules through the electric force (S1.9), which ultimately leads

to non-negligible disturbances of the hydrodynamic field around the diffusion flame, as described below.

The temperature T along the axis of the burner in the presence of electric fields is shown in Fig. 5. It is worth mentioning that the maximum temperature undergoes only small variations in all cases, although the location of the peak fluctuates around the unelectrified one in a manner that does not appear to have a straightforward explanation. Note that, as shown in Sec. 3.4, the flow in the vicinity of the axis becomes increasingly two-dimensional as the voltage increases because of the fluid-mechanical disturbances introduced by the electric force, which complicates the interpretation of the complex patterns of variations observed along the burner axis. As the voltage is increased, the temperature profile widens and the peak increases as a result of a decrease in the strain rate and of an increase in the current across the burner, the latter inducing a small Ohmic dissipation [i.e., the last term on the right-hand side of Eq. (S1.5)] that in the present operating conditions can only heat up by a few degrees the cold flow of gases on both sides of the mixing layer. The phenomenon contributing to the displacement and the shape modification of the axial profiles, including the cause of the decrease in the strain rate, involves the interaction of ionic winds with the incoming flow of the neutral mixture and is discussed further below.

In the diluted case $Z_{st} = 0.50$ provided in Fig. 5b, the location of the temperature peak remains mostly the same independently of the applied electric field, and the temperature increment on the flanks of the mixing layer is less intense. In contrast to the non-trivial pattern of variations observed in the undiluted case in Fig. 5a, the curves in the diluted case can be easily grouped into subsaturated (i.e. 0.0, -0.5, and $-1.0\,\mathrm{kV}$) and saturated (i.e. $-1.5\,\mathrm{kV}$ and $-2.0\,\mathrm{kV}$) subsets indicating a negligible shift of the temperature peak as the voltage increases. The decreased shift of the profiles and the collapse of the curves into those two subsets are observed as well in other bulk quantities such as major neutral concentration profiles, flow velocities and scalar dissipation rates, as shown later in Sec. 3.4.

The general structure of the concentration profiles of major reactants and products undergoes very small variations under the sub-breakdown electric fields studied here. This is shown in Fig. 6, which provides the profiles of molar fractions X_i of the major neutral species CH_4, O_2 and H_2O along the burner axis. The CH_4 is attacked by H radicals in the diffusion flame in a chain-breaking reaction to form CO, which oxidizes to CO_2 in a broader oxidation layer that lays on the O_2-side of the diffusion flame (profiles not shown here for brevity). The overall effect of the electric field is to spatially shift these profiles in a manner analogous to that observed for the temperature in Fig. 5. Concurrent with the latter, a broadening of the mixing layer is observed in Fig. 6 as the voltage increases due to the temperature-induced increase in the kinematic viscosity.

A minor but relevant intermediate included in Fig. 6 is CH, which, together with O, participates in the chemi-ionization step $CH + O \longrightarrow CHO^+ + e^-$ that starts the ionic-chemistry pathways. In all cases, the CH layer is thin (it is computationally solved by ~ 8 grid points), and is spatially located closer to the fuel side of the diffusion flame. As the applied voltage increases, the peak molar fraction of CH, which is of order 10^{-5}-10^{-6}, decreases and shifts in accordance with the temperature and the profiles of the other major neutral species displayed in the figure. In the fuel-diluted case $Z_{st} = 0.50$, the modifications introduced by the electric field in the species profiles in Fig. 6b are qualitatively consistent with the experimen-

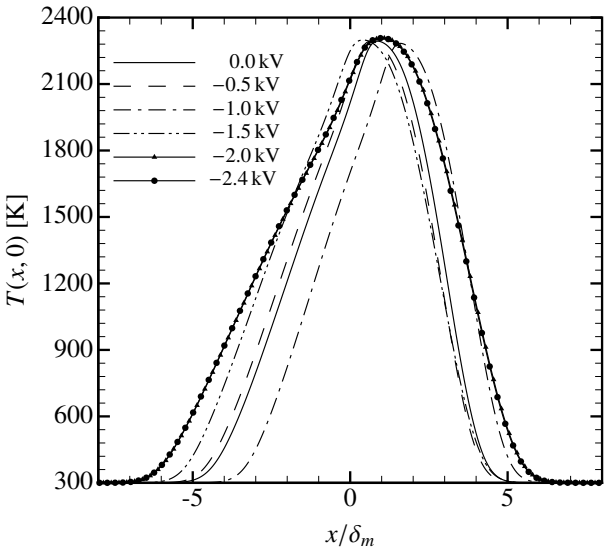

(a)

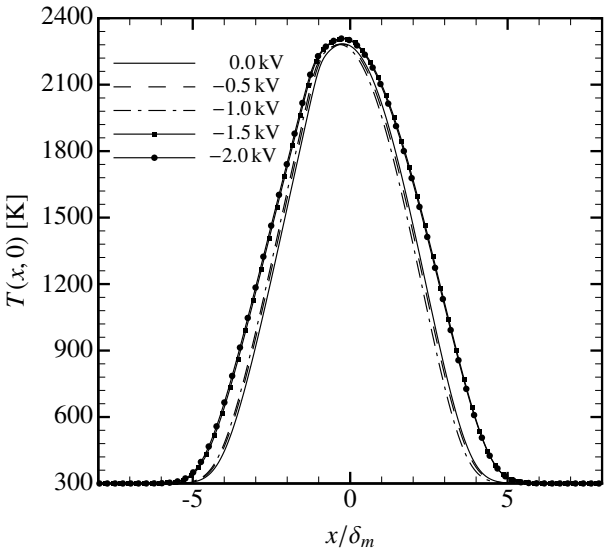

(b)

Figure 5: Temperature profiles along the axis of the burner for (a) $Z_{st} = 0.07$ and (b) $Z_{st} = 0.50$. The curves for -2.0 and -2.4 kV (in panel a) and -1.5 and -2.0 kV (in panel b) are almost coincident.

tal observations on the flame axial position based on flame luminosity in Park *et al.* [1] (note however that direct comparisons of the present simulations with those observations are not pursued since the chemical mechanism cannot reproduce radiative excited species). Specifically, the distributions in the two top panels in Fig. 6b, which correspond to sub-saturated conditions, are almost coincident. The same is observed in the two bottom panels where the diffusion flame reaches electrical saturation. In these two saturated cases, the diffusion flame is slightly shifted towards the fuel side relative to the subsaturated cases, and a decrease in CH molar fraction occurs in a similar manner as in the undiluted case in Fig. 6a. Once saturation conditions are attained, it is shown below in Sec 3.4 that the local strain rate in the vicinity of the flame location decreases as a result of the flow displacement created by the ionic wind, and, as a consequence, the local diffusion time increases, thereby elevating the peak temperature albeit in small amounts, as observed in Fig. 5. The subsequent attainment of increasingly faster overall chemistry generally decreases the content of all intermediates, including CH and the ionized species, as shown below.

The axial distributions of molar fractions of the six charged species participating in the ionic chemical description provided in S1.2, namely H_3O^+, CHO^+, $O_2{}^-$, O^-, OH^-, and e^-, are shown in Fig. 7 along the burner axis. It is worth mentioning that, under zero incident electric fields, as in the top left panels of Figs. 7a and b, there exists a self-induced, quasi-electroneutral distribution of charged species in the diffusion flame that nonetheless leads to vanishingly small potentials of order 10 V, which are caused by small mismatches between hydronium and electron concentrations. The general structure of the charged species in the unelectrified cases, however, reveals some important physical phenomena that are disturbed when the external voltage is applied. In particular, for $\Delta\Phi_0 = 0$, it is observed that the H_3O^+ produced by the charge-transfer reaction $CHO^+ + H_2O \longrightarrow H_3O^+ + CO$ represents the major ion in the diffusion flame, whose peak concentration location coincides with that of CH in Fig. 6. In contrast, the CHO^+ produced by the chemi-ionization step $CH + O \longrightarrow CHO^+ + e^-$ is present only in relative fractional amounts as a result of its rapid conversion into H_3O^+ through the step $CHO^+ + H_2O \longrightarrow H_3O^+ + CO$. The molar fraction of hydronium is mostly everywhere matched by that of the electrons, which are present in the mixture in peak number-density amounts of order $10^{11}\,\mathrm{cm}^{-3}$. Consequently, the positive charge of H_3O^+ is correspondingly neutralized, with small positive differences of order $X_{H_3O^+} - X_{e^-} = O(10^{-12})$ being responsible for the small self-induced voltages as a result of the larger diffusivity of the electrons. However, near the oxidizer side, the concentration of electrons decreases rapidly and is unaccompanied by a decrease in H_3O^+, as it would be expected if the process involved the dissociative recombination reaction $H_3O^+ + e^- \longrightarrow H_2O + H$. Instead, the electrons are invested in the attachment steps $O_2 + e^- + M \longrightarrow O_2{}^- + M$, $OH + e^- + M \longrightarrow OH^- + M$, and $O + e^- + M \longrightarrow O^- + M$, which produce the major participating anions $O_2{}^-$, OH^-, and O^-. Eventually, these heavy anions are responsible for the portion of the bi-directional ionic wind that flows in the direction opposite to the incident electric field.

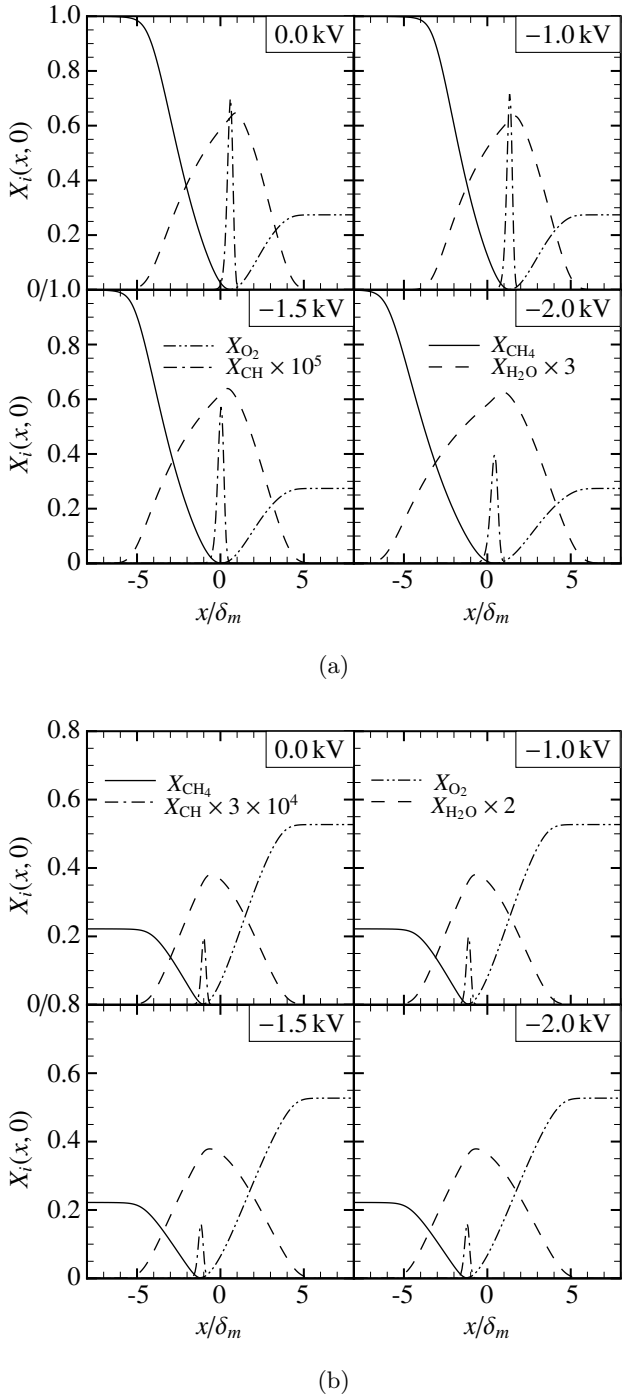

Figure 6: Molar fraction profiles of the neutral species along the axis of the burner for (a) $Z_{st} = 0.07$ and (b) $Z_{st} = 0.50$.

Upon applying an external electric field in the $-x$ direction, Fig. 7 indicates that H_3O^+ and –to a much lesser extent– CHO^+ are steered toward the cathode while the

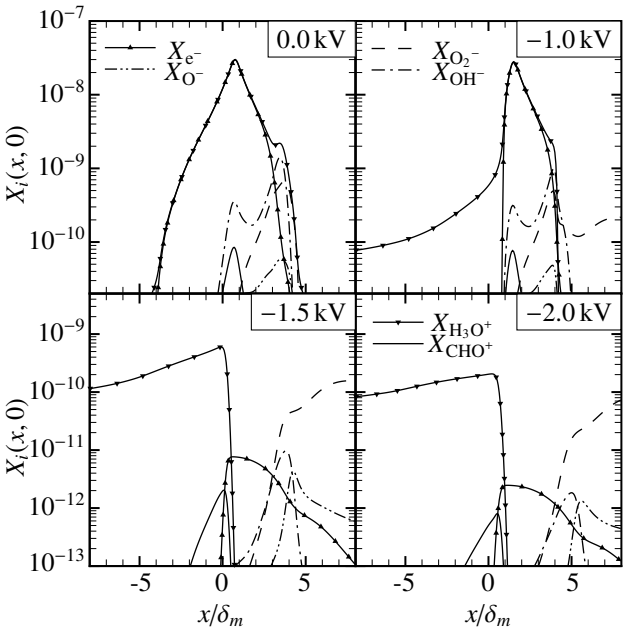

(a)

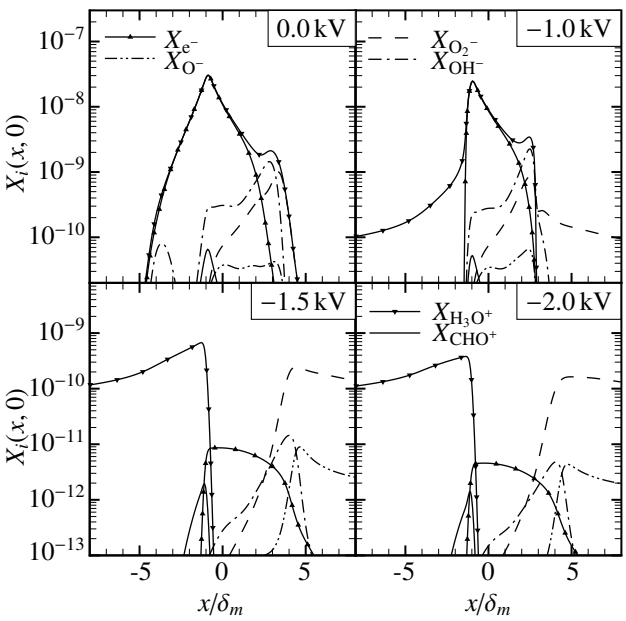

(b)

Figure 7: Molar fraction profiles of charged species along the axis of the burner for (a) $Z_{st} = 0.07$ and (b) $Z_{st} = 0.50$.

cloud of negative charges is steered toward the anode. It is worth highlighting that the chosen polarity of the electric field efficiently leads to this distortion as opposed to a field applied in the $+x$ direction, in that the negative charges are prominently produced on the oxidizer side of the flame and therefore can be easily steered toward an anode placed on that side. Among the negative charges, the $O_2{}^-$ overwhelmingly dominates the charged concentration profiles on the oxidizer side in both undiluted and diluted cases because of the prevalence of O_2 there, which mediates in the production of $O_2{}^-$ through the electron-attachment reaction $O_2 + e^- + M \longrightarrow O_2{}^- + M$.

Below the voltage for the onset of the overcurrent in Fig. 4a, the central distribution of charged species in the diffusion flame is marginally influenced by the incident electric field, as shown in the right upper panel in Fig. 7a. In this way, the net electric charge density remains everywhere small in this region. However, a noticeable electric drift of ions occurs that creates long tails in the distributions of molar fractions of H_3O^+ and $O_2{}^-$ lasting up to the surfaces of the electrodes. As a result, positive and negative charge imbalances occur, respectively, on the fuel and oxidizer sides of the mixing layer, which, in conjunction with the decreasingly small values of ionic mobilities attained as low temperatures are approached in the periphery of the flame, lead to the charge density spikes shown in Fig. 3 and to the subsequent screening of the incident electric field. Additionally, as explained later in Sec. 3.3, this excess of ions outside the mixing layer, which is accompanied by an outwardly motion as prescribed by the incident electric field, is responsible for the bi-directional ionic wind, the alteration of surrounding hydrodynamic field along distances of order L, and the modification of the flame axial position in the burner.

In saturated conditions corresponding to the bottom panels in Figs. 7a and b, the amount of produced charges is not sufficiently large to shield the reacting region from the incident electric field. In these conditions, the electric field is able to steer a large amount of charged species away from the reaction zone before they are replenished by their corresponding production steps. This leads to the occurrence of an upper limit in the ion current across the burner, as shown in Fig. 4. As a consequence, a large decrease (i.e., by one to two orders of magnitude) in the molar fraction of charged species in the diffusion flame is observed with increasing voltages. On the other hand, the concentration of charges near the electrodes is relatively more robust to variations in the voltage.

The depletion of electrons in the diffusion flame predicted as the voltage is increased beyond sub-saturation conditions is comparatively more evident than for other ions because of the large values of the electron mobility μ_{e^-} (see Sec. S1.3 of the Supplementary Material for details on the calculation of mobilities of charged species). In particular, the electrons undergo a fast depletion once transported to the oxidizer edge of the mixing layer, where they are rapidly transformed into other anionic species through electron-attachment reactions. In addition, as the voltage increases, the increasing drift of electrons towards the anode inhibits the spatial overlap between the $X_{H_3O^+}$ and X_{e^-} distributions, which largely suppresses the dissociative recombination step $H_3O^+ + e^- \longrightarrow H_2O + H$. Consequently, this favors the onset of saturation, in which the removal of charged species relies on the electric drift towards the electrode.

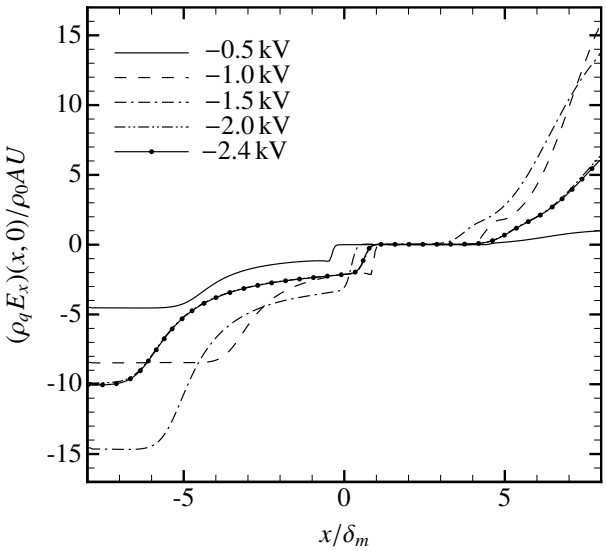

(a)

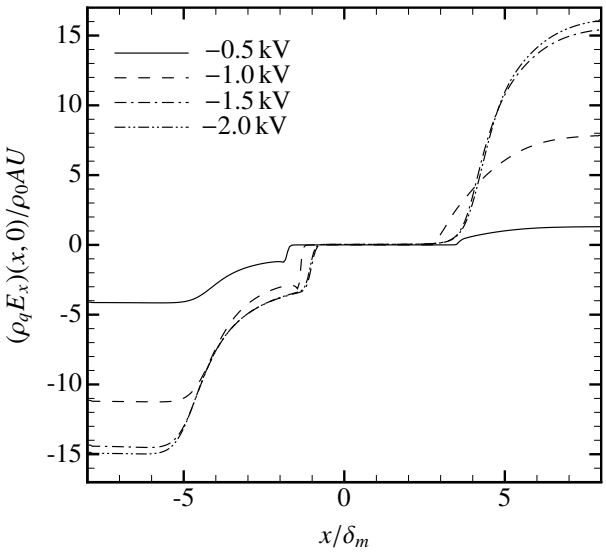

(b)

Figure 8: Axial component of the non-dimensional electric force profiles along the axis of the burner for (a) $Z_{st} = 0.07$ and (b) $Z_{st} = 0.50$. In panel (a), the lines corresponding to -2.0 and -2.4 kV are almost coincident.

3.3. Distribution of electrically-induced ionic winds

The incident electric field induces a displacement of charges axially outwards from the flame, as quantitatively shown in Figs. 3 and 7. In particular, the major ions that prevail on the fuel and oxidizer sides are, respectively, H_3O^+ and $O_2{}^-$, which have similar mobilities. Despite the small sub-ppm concentration of these ions near the electrodes, an electric force $\mathbf{f}_{el}$ given by (S1.9) that scales with the characteristic convective acceleration $\rho_0 AU$ of the flow outside the mixing layer is generated across the burner on both oxidizer and fuel streams, as shown in Fig. 8 for both undiluted and diluted cases, and in accordance with the order-unity values selected for the dimensionless interaction parameter Ξ in Eq. (1). This force, which gives rise to the bi-directional ionic wind, acts primarily in the axial direction and tends to displace the gas axially outwards away from the diffusion flame. This flow-displacement effect is favored by the lower temperatures and correspondingly larger values of the mixture density outside the mixing layer.

As indicated by its definition (S1.9), the electric force $\mathbf{f_{el}}$ is given by the multiplication of the charge density ρ_q by the electric field $\mathbf{E}$. In particular, the variations of $\mathbf{f_{el}}$ with the applied voltage in Fig. 8 are qualitatively similar to those of the electric charge in Fig. 3. In the undiluted case, the electric force increases with the applied voltage in most of the spatial domain up to the overcurrent voltage $-1.5\,\mathrm{kV}$. Saturated conditions are attained for $-2.0\,\mathrm{kV}$ that flatten and broaden the charge distribution and the electric-force profile. Under fuel dilution, the electric force also increases monotonically almost everywhere with the applied voltage, as shown in Fig. 8b. In all cases, and in the scales of the vertical axis utilized to draw Fig. 8, a plateau of vanishingly small values of $\mathbf{f_{el}}$ is observed in the electric force that coincides spatially with a similar plateau of vanishing electric charge observed in Fig. 3, and which corresponds to the layer where the chemical reactions in the diffusion flame develop.

In connection with the effect of the incident electric field on the bulk flow, a qualitative aspect worthy of discussion is the asymmetry of the electric-force profiles with respect to the flame. For instance, the undiluted case in Fig. 8a is characterized by a clear asymmetry in the profiles that is induced by the tendency of chemical reactions to develop closer to the oxidizer side because there is where overall stoichiometric conditions occur. In contrast, the fuel-diluted case in Fig. 8b has a comparatively more symmetric distribution of electric force. Asymmetric profiles of ionic winds as in Fig. 8a lead to more significant distortions of the position of the stagnation plane, which is pushed downwards to the fuel side. Electrically-induced disturbances of the flow field are analyzed in the following section.

3.4. Effects of the incident electric field on the aerodynamics and mixing of reactants

The numerical results presented above provide evidence of a bi-directional ionic wind that is directed outwards from the diffusion flame and which emerges from the distortion induced by the incident electric field on the distribution of charged species. The transfer of momentum from the ionic wind to the bulk gas is significant and generates modifications of the velocity and mixing fields, as shown below.

A first evidence of this electrically-induced hydrodynamic phenomenon in both diluted and undiluted cases is shown by the axial distributions of axial velocities provided in Fig. 9. Consider first the undiluted case in Fig 9a. The

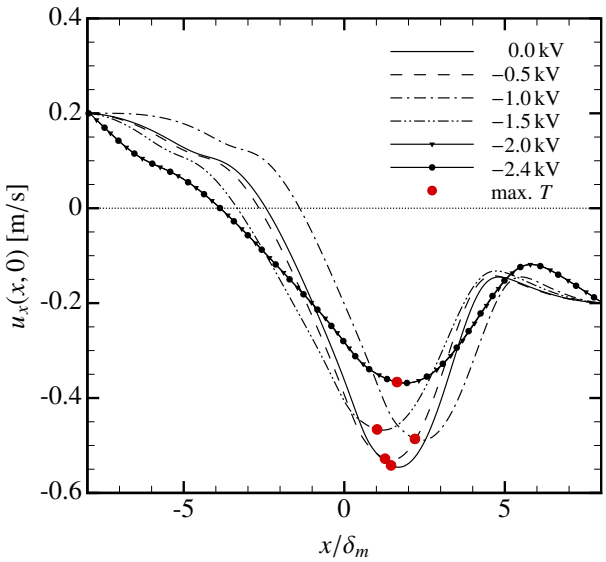

(a)

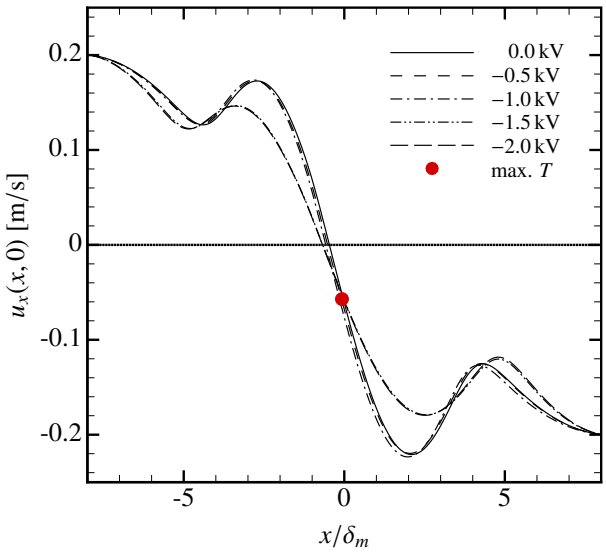

(b)

Figure 9: Axial velocity profiles along the axis of the burner for (a) $Z_{st} = 0.07$ and (b) $Z_{st} = 0.5$. The red dots indicate the position of the maximum of the axial profile of temperature. The curves for -2.0 and -2.4 kV (in panel a) and -1.5 and -2.0 kV (in panel b) are almost coincident. In panel (b) the red dots are almost coincident for all curves.

velocity profile in the unelectrified case differs from the quasi-linear one expected in constant-density non-reacting flows, in that it displays a rapid acceleration of the axial flows of fuel and oxidizer towards the flame due to thermal expansion. As shown in Fig 9a, the maximum temperature is located to the left of the axial-velocity maximum. Incrementing the voltage across the sub-saturated conditions from $|\Delta\Phi_0| = 0.5$ to 1.0 kV has the effect of displacing the diffusion flame jointly with the stagnation plane first toward the fuel side and then toward the oxidizer side without extensive deformation of the axial velocity profile along the burner axis and in a manner that correlates well with the shifts in the temperature profiles in Fig. 5. Two-dimensional visualizations of these variations are provided in Fig. 10, which shows flow streamlines along with contours of CH mass fractions. In interpreting these two cases, it is worth noting that the shift toward the oxidizer side in the -1.0 kV case is actually the result of a significant convex curvature of the stagnation plane, which curves downwards as the ionic wind pushes it toward the fuel side as observed in the second panel in Fig. 10. At the overcurrent voltage, $|\Delta\Phi_0| = 1.5$ kV, the stagnation plane moves farther to the fuel side jointly with the flame, but the axially outwards flow displacement made by the increasingly stronger ionic wind makes the axial velocity profile shallower, thereby decreasing the effective strain rate in the flame vicinity. Correspondingly, the stoichiometric value χ_{st} of the scalar dissipation rate

$$\chi(Z) = 2D_Z|\nabla Z|^2, \tag{3}$$

evaluated at $Z = Z_{st}$, decreases by approximately 50% as the voltage is increased to the saturation value, as shown in Fig. 11. The resulting deficit of charged species caused by the faster overall chemistry leads to the non-monotonic trend of the electric intensity with the applied voltage observed in Fig. 4a.

In Eq. (3), the diffusivity D_Z is taken equal to the local thermal diffusivity of the mixture. Additionally, as proposed by Pitsch and Peters [36] and standardly done in flamelet modeling, Z is a mixture fraction obtained by computing the solution to the sourceless advection–diffusion equation

$$\nabla \cdot (\rho \mathbf{u} Z) = \nabla \cdot (\rho D_Z \nabla Z) \tag{4}$$

subject to $Z = 0$ and $Z = 1$ on the oxidizer and fuel streams, respectively, with zero normal-gradient conditions being applied everywhere else along the boundaries of the computational domain. A reference scalar dissipation rate can be obtained by integrating (4) assuming negligible variations of Z in the radial direction, constant values for ρ and D_Z, infinitely far boundaries located at $x \to \pm\infty$, along with a linear velocity distribution $u_x = -Ax$. The resulting expression is [11, 37]

$$\chi(Z) = \frac{A}{\pi} \exp\left\{-\left[\sqrt{2}\mathrm{erfc}^{-1}(2Z)\right]^2\right\}, \tag{5}$$

which corresponds to a symmetric bell-shaped curve centered at $Z = 0.5$.

The reference scalar dissipation rate in Eq. (5) is compared in Fig. 12 to the scalar dissipation arising from the numerical solution of Eq. (4) for the present problem. Note that the scalar dissipation rate of the unelectrified case does not match the reference value (5) due to the temperature dependence of D_Z and to thermal-expansion effects.

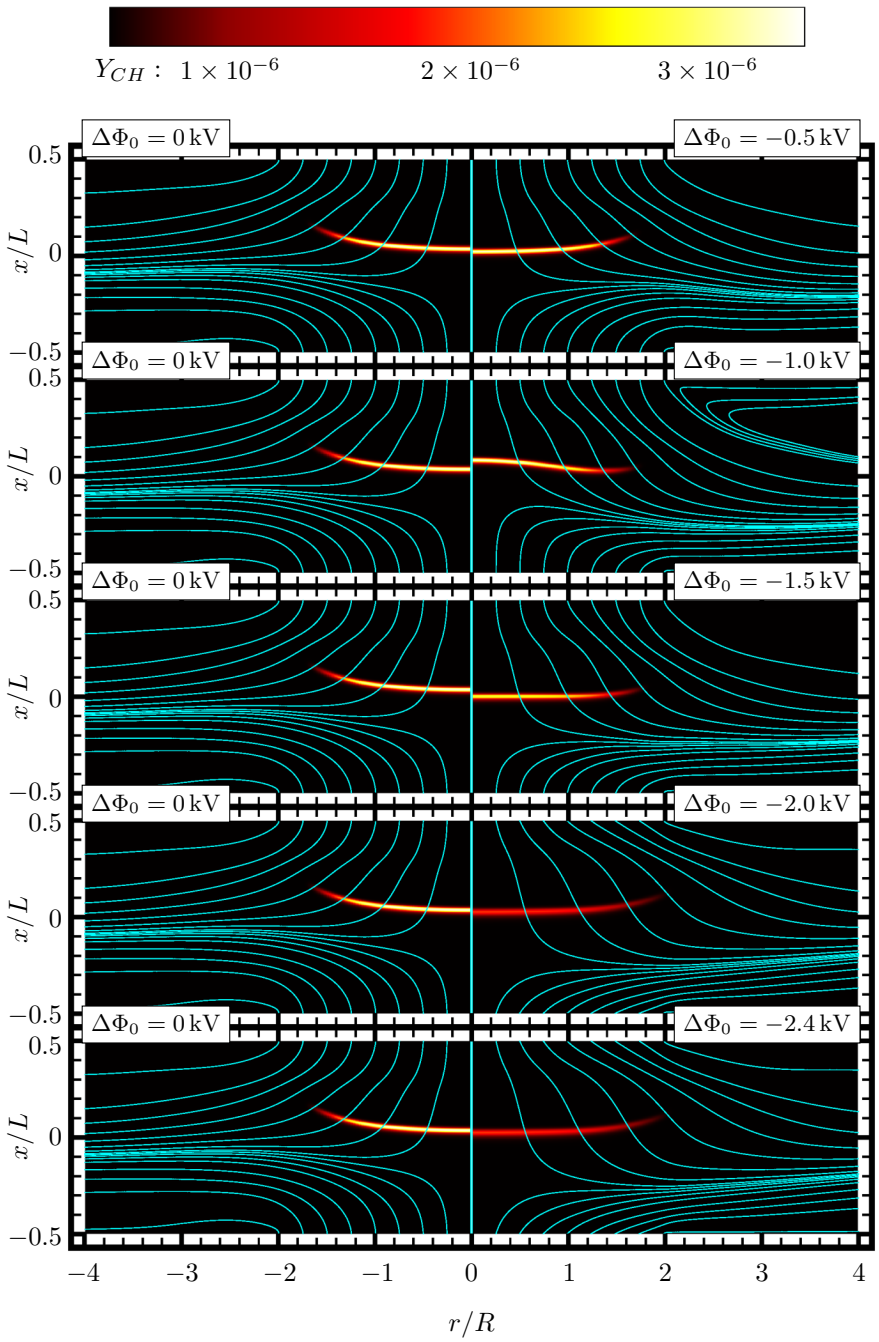

(a)

Figure 10: Flow streamlines overlaid on CH mass-fraction contours for $Z_{st} = 0.07$. The unelectrified case $\Delta\Phi_0 = 0\,\mathrm{kV}$ is provided on the left panels to facilitate direct comparison with the corresponding electrified case.

More importantly, in the undiluted case in Fig. 12a, as the voltage is increased, the scalar dissipation rate becomes increasingly skewed to the fuel side due to the augmentation of composition gradients there as a result of the downward displacement of the stagnation plane.

As saturation conditions are approached, $|\Delta\Phi_0| \geq 2.0\,\mathrm{kV}$, the strength of the ionic wind becomes limited by the rate of production of charged species. In this limit, an equilibrium configuration is attained in a strain-rate field that shows little to no sensitivity to the applied voltage, as shown by the lower plateau attained by the stoichiometric scalar dissipation rate in Fig. 11.

The hydrodynamic interactions described above are much more limited in the fuel-diluted case $Z_{st} = 0.50$, which

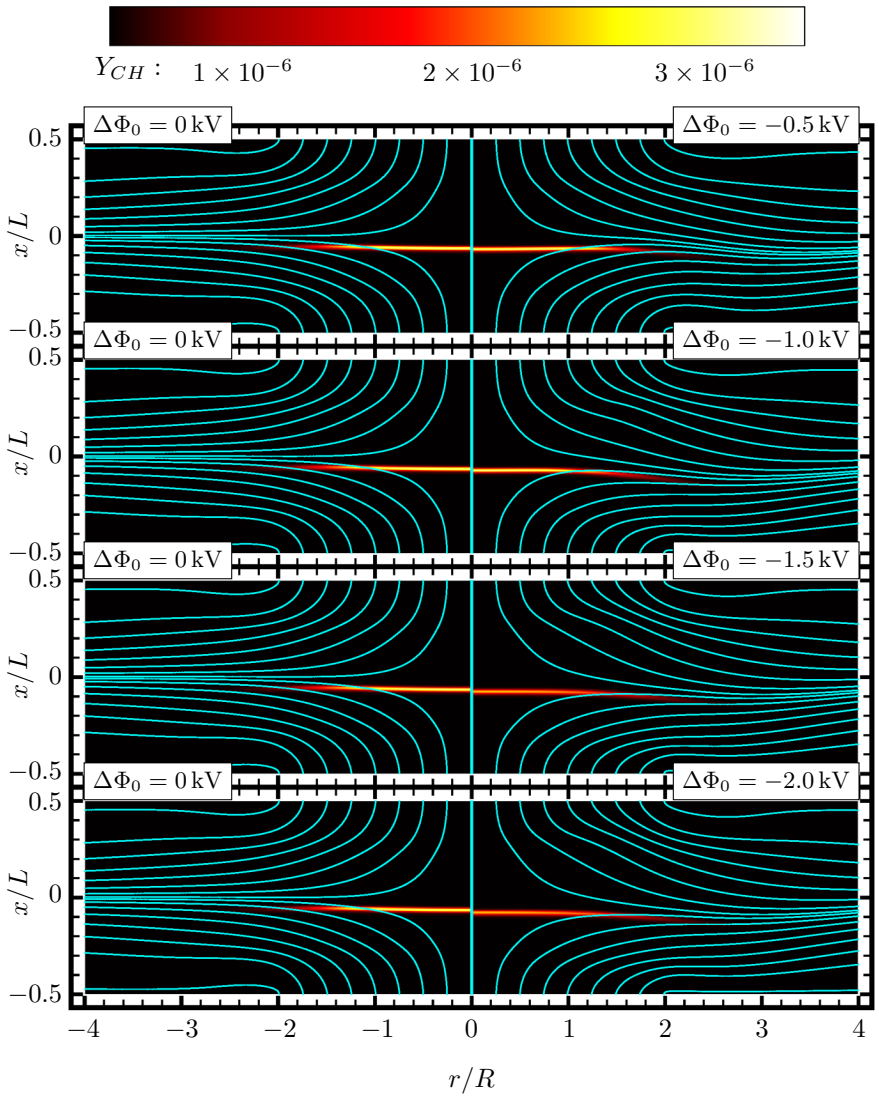

(b)

Figure 10 (Continued): Flow streamlines overlaid on CH mass-fraction contours for $Z_{st} = 0.50$. The unelectrified case $\Delta\Phi_0 = 0\,\mathrm{kV}$ is provided on the left panels to facilitate direct comparison with the corresponding electrified case.

generally leads to a diffusion flame positioned closer to the stagnation plane as required by the modified spatial location of the stoichiometric conditions. The resulting axial velocity profile remains mostly symmetric about the mid section of the burner, as shown in Fig. 9b. In addition, the increased symmetry of the electric force, in this case leads to negligibly small shifts of the position of the stagnation plane, as observed in the two-dimensional visualizations in Fig. 10. Although the overall effect of the incident electric field at saturation is to decrease χ_{st} by approximately 30%, the distribution of the scalar dissipation rate in mixture-fraction space remains close to that of the unelectrified case, as shown in 12b.

3.5. Comparisons with experimental flow fields

The experimental flow visualizations by Park *et al.* [1] suggest strong modifications of the velocity field at similar voltages to the ones addressed in this study. In contrast, the numerical results presented here indicate that the modifications are rather moderate. This section provides a brief discussion about possible sources of these discrepancies.

A comparison between experimental and numerical profiles of the axial velocity are provided in Fig. 13 for the undiluted case $Z_{st} = 0.07$. Although the general trends of both experimental and numerical profiles are the same as the voltage is increased, including the axial shift of the stagnation plane toward the fuel side, the comparisons re-

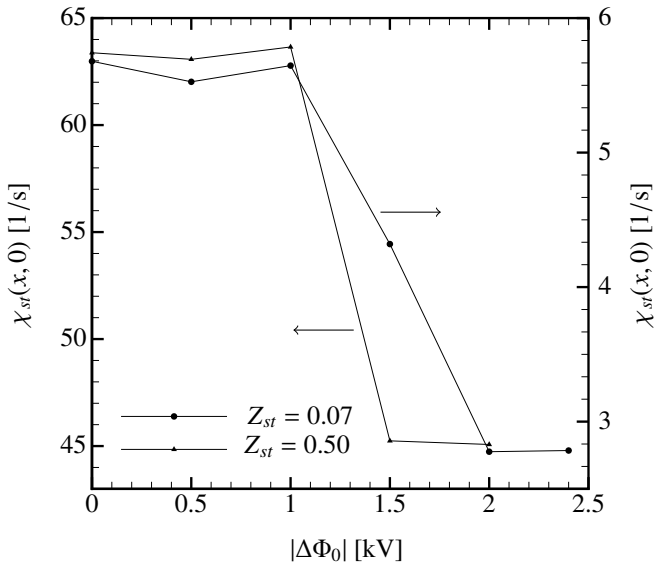

Figure 11: Stoichiometric scalar dissipation rate as a function of the applied voltage.

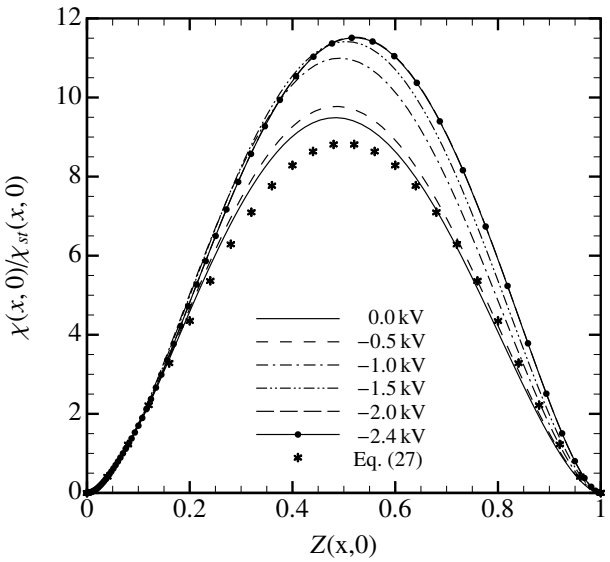

(a)

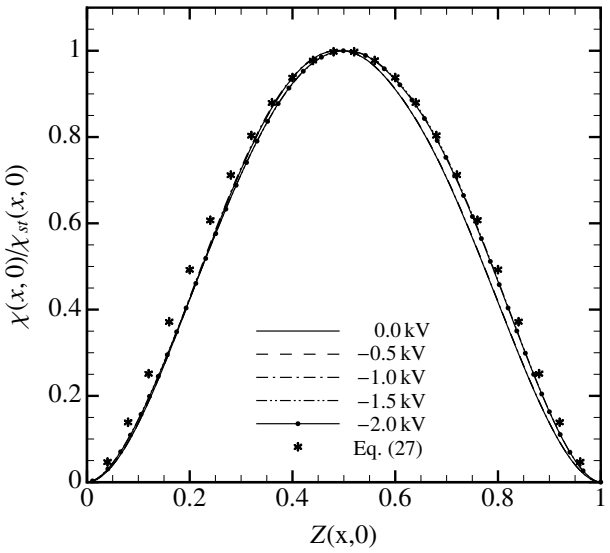

(b)

Figure 12: Normalized scalar dissipation rate profiles as a function of the mixture fraction along the axis of the burner for (a) $Z_{st} = 0.07$ and (b) $Z_{st} = 0.50$. The curves for -2.0 and -2.4 kV (in panel a), 0.0, -0.5 and -1.0 kV (in panel b), and -1.5 and -2.0 kV (in panel b) are almost coincident.

veal significant quantitative discrepancies. The first noteworthy aspect relates to the first experimental point near the fuel orifice, where the measured velocity is approximately 10 cm/s larger than the numerical one, despite the fact that the fuel mass flow rate was experimentally controlled in Ref. [1] to yield the same value of injection velocity as the one utilized in the present study. This mismatch may be caused by the area constriction of the holes on the perforated plate and the corresponding local acceleration of the flow there [38].

A second important aspect of the comparison made in Fig. 13 relates to the discrepancies in the electrified cases, where the numerical values of the axial velocity on the oxidizer side are significantly larger than the experimental ones. In particular, the smaller values observed in the experiments appear to be linked with the significant flow blockage caused by the ionic wind on the oxidizer side, which, in the experimental cases utilizing propane as fuel, may even lead to the occurrence of a second stagnation plane near the oxidizer injector (e.g., see Fig. 5e in Ref. [1]). However, such intense flow modifications were not observed in the present study. One possible cause of these differences could be related to the effects of the electric charge inadvertently acquired by the tracer particles employed in the PIV to measure experimentally the axial velocity profiles. To see this, consider a number of inertial point particles of TiO_2 with similar physical properties to those used in the experiments by Park *et al.* [1], and which are to be seeded below one-way coupled into the numerical flow fields in a manner analogous to the role played by the PIV tracers in the experiments. In particular, the particles are characterized by their radius $a_p = 0.1\,\mu$m, material density $\rho_p = 4230\,\mathrm{kg/m^3}$, and electric charge q_p, the latter being treated here as an adjustable parameter since it cannot be easily measured. The associated aerodynamic Stokes number of the particles is $\mathrm{St}_{ae} = (2/9)(\rho_p/\rho_0)a_p^2 A/\nu_0 \sim 5\times10^{-4} \ll 1$, indicating that they are mostly tracers of the flow field in conditions where their electric charge is negligible.

The position of the simulant PIV particles, $\mathbf{x}_p$, is computed from the trajectory equation

$$\frac{d\mathbf{x}_p}{dt} = \mathbf{u}_p, \tag{6}$$

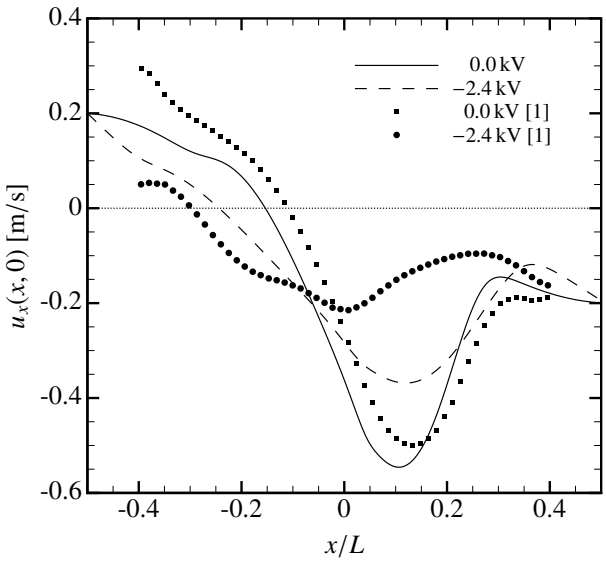

Figure 13: Comparison between numerical simulations (lines) and experimental measurements by Park *et al.* [1] (symbols) of the axial velocity profiles along the axis of the burner for $Z_{st} = 0.07$.

where the velocity of the particles, $\mathbf{u}_p$, is obtained by integrating the second Newton's law

$$\frac{4}{3}\pi\rho_p a_p^3 \frac{d\mathbf{u}_p}{dt} = 6\pi\rho(\mathbf{x}_p)\nu(\mathbf{x}_p)a_p\left[\mathbf{u}(\mathbf{x}_p) - \mathbf{u}_p\right] + q_p\mathbf{E}(\mathbf{x}_p) \tag{7}$$

individually for every particle. In Eq. (7), the last term on the right-hand side refers to the electric force exerted on a charged particle by the incident electric field, which in principle makes the particle depart from the trajectories followed by a fluid particle. Additionally the symbol "$(\cdot)(\mathbf{x}_p)$" is associated with the evaluation of the corresponding Eulerian field at the position of the particle. This evaluation is performed using a bi-linear interpolation inside the grid cell containing the particle. Interactions between particles, and between particles and the flow, are neglected because of the high dilution employed. The particles are seeded in kinematic equilibrium with the flow at the fuel and oxidizer orifices. The values of q_p employed in the simulations are $q_p = \pm 10^{-17}$ C for $Z_{st} = 0.07$, and $q_p = \pm 1.6 \times 10^{-17}$ C for $Z_{st} = 0.50$, which amount approximately to just 200 elementary charges per particle, with positive and negatively charged particles being injected at the fuel and oxidizer inlets, respectively.

Figure 14 provides the trajectories $\mathbf{x}_p$ of the simulant PIV particles obtained by simultaneously integrating Eqs. (6)-(7), and illustrates the sensitivity of the solution to the electric charge q_p. For instance, for zero charge, the particles become tracers of the flow field independently of the applied voltage, as easily observed by comparing the right panels in Figs. 10 with those in Fig. 14. In contrast, when the particles are charged, their trajectories differ significantly from the flow streamlines in both undiluted and diluted cases, as observed in the left panels in Fig. 14. Note

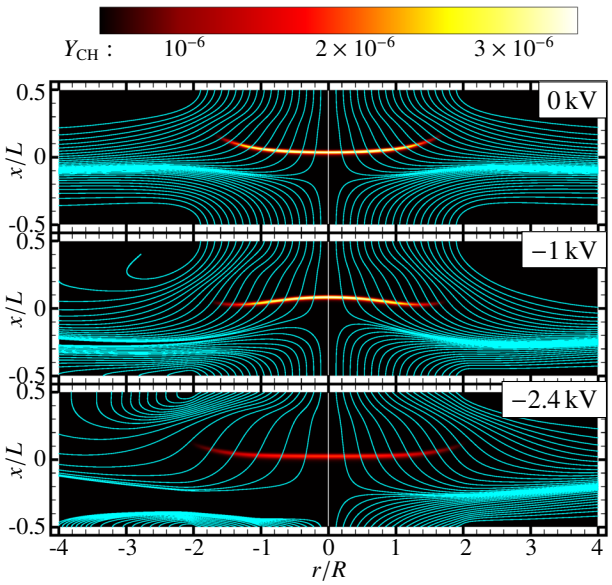

(a)

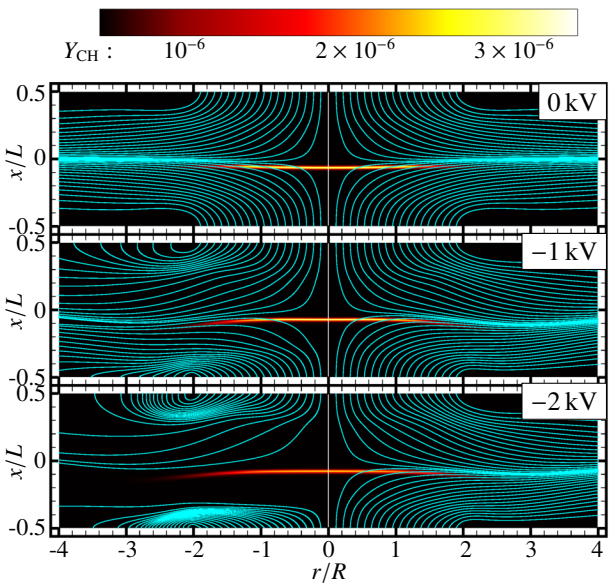

(b)

Figure 14: Simulant PIV particle trajectories $\mathbf{x}_p$ overlaid on CH mass-fraction contours for (a) $Z_{st} = 0.07$ and (b) $Z_{st} = 0.50$. The trajectories corresponding to uncharged tracers are provided on the right side of each panel about the symmetry axis of the burner, while the trajectories for the charged (non-tracer) particles are provided on the left side of each panel.

that the particle charge has been chosen in such a way that, at high voltages, it leads to comparable values of the characteristic electric force on the particles, $q_p|\Delta\Phi_0|/L$, and the viscous force on the particles $6\pi\rho_0\nu_0 a_p U$ based on the flow injection velocity. The ratio of these two forces, which can also be expressed as the ratio of the electro-migration velocity $|q_p||\Delta\Phi_0|/(6\pi\rho_0\nu_0 a_p L)$ to the characteristic flow

velocity U, is associated with the electric Stokes number

$$\mathrm{St}_{el} = |q_p||\Delta\Phi_0|/(6\pi\rho_0\nu_0 a_p U L), \tag{8}$$

whose values are within the range $\mathrm{St}_{el} \sim 0.07 - 0.34$ in the present calculations, with the largest values being produced by the highest voltages tested here. As a consequence, as the voltage increases, the electric force becomes of the same order as the aerodynamic force on the particles outside the mixing layer. As shown in Fig. 14, this particular choice of parameters leads to rolled-up trajectories of the negatively charged particles injected on the oxidizer side, creating a pattern of fictitious streamlines that curves upwards (on the oxidizer side) and downwards (on the fuel side) and is reminiscent of the ones observed in the experiments (e.g., see Fig. 12b in Ref. [1]). These considerations highlight the outstanding challenges related to performing PIV in the type of electrified flows studied here, in which a rather small amount of electric charge attached to the tracer particles can deflect their trajectories and turn them into non-tracers.

4. Conclusions

In this study, axisymmetric numerical simulations of methane-air counterflow laminar diffusion flames impinged by sub-breakdown DC electric fields are performed using multi-component transport and a detailed chemical mechanism that includes elementary steps for the conversion of six electrically charged species. An axial electric field is induced by two electrodes located on the oxidizer and fuel sides and arranged parallel to the mixing layer. The configuration matches the geometry and flow parameters of the burner recently studied experimentally by Park *et al.* [1]. Steady-state solutions are obtained by integrating the conservation equations using a pseudo-time stepping method.

The overall effect of the incident electric field is to induce a bi-directional ionic wind that interacts with the two incoming streams of neutral gases, in such a way that the local strain rate is decreased. This generates a faster-burning flame and, consequently, a smaller concentration of charged species. Byproducts of this phenomenon are a slight increase in the flame temperature, a decrease in the stoichiometric scalar dissipation rate, a displacement of the stagnation plane, a non-monotonic trend of the electric intensity with respect to the applied voltage, and a strong distortion in the spatial distribution of charged species.

In the present arrangement of the electrodes, where the upper one in the oxidizer stream is the anode, and the bottom one in the fuel stream is the cathode, the ionic wind is primarily composed of O_2^- ions flowing to the oxidizer side, and H_3O^+ ions flowing to the fuel side. The transfer of momentum between the ionic wind and the neutral gases occurs primarily outside the mixing layer in the fuel and oxidizer streams. In contrast, the hot gas within the diffusion flame tends to move under quieter conditions of quasi-electroneutrality and negligibly small electric force. Fuel dilution tends to dampen these effects by centering the diffusion flame in the burner, which leads to an increased cancellation of the electric forces induced by the ionic winds.

At small voltages, the diffusion flame behaves as a quasi-perfect conductor whose interior is shielded by electric charges produced in abundance, while high voltages enhance dispersion of charges and lead to saturation of the electric current. An intermediate regime, where an overcurrent occurs, is found that results from the competition between electric drift, charge production, and molecular diffusion of reactants.

The results presented in this study are in qualitative agreement with the experimental observations made by Park *et al.* [1]. Nonetheless, quantitative disagreements are obtained in the saturation current, which is larger in the simulations, and in the intensity of the flow modifications enabled by the incident electric field, which are more pronounced in the experiments. The former issue calls for necessary improvements in the chemical-kinetic description of the problem and in the transport description of ionized species, while the latter involves experimental uncertainties related to hydrodynamic effects caused by the perforated plates and to the fundamental question of whether the PIV tracers follow the flow pathlines in the presence of incident electric fields. In the present work, calculations of trajectories of simulant PIV particles carrying a small amount of electric charge, which nonetheless makes them to be non-tracer particles, show improved agreement with experimentally observed flow patterns.

The functional form of the scalar dissipation rate is found to depend on the applied electric field. This suggests that a closure model for the scalar dissipation rate, to be used in notional subgrid-scale flamelet models incorporating these effects, should in principle be augmented to account for the resolved value of the electric field. The extent to which useful calculations can be made neglecting this functional dependence is subject of future work.

Acknowledgments

This investigation has been supported by the US AFOSR Grant # FA9550-14-1-0219, the Italian Apulia Space Grant # PON03PE_00067_6, and the US DoE/NNSA Grant # DE-NA0002373 as part of the Stanford PSAAP-II Center. This work was performed during the visit of the first author to the Stanford University Center for Turbulence Research during Fall 2016 and Winter 2017.

References

[1] D. G. Park, S. H. Chung, M. S. Cha, Bidirectional ionic wind in nonpremixed counterflow flames with DC electric fields, Combustion and Flame 168 (2016) 138–146.

[2] J. Lawton, F. J. Weinberg, Maximum Ion Currents from Flames and the Maximum Practical Effects of Applied Electric Fields, Proceedings of the Royal Society of London A: Mathematical, Physical and Engineering Sciences 277 (1964) 468–497.

[3] A. Fialkov, Investigations on ions in flames, Progress in Energy and Combustion Science 23 (1997) 399–528.
[4] S. D. Marcum, B. N. Ganguly, Electric-field-induced flame speed modification, Combustion and Flame 143 (2005) 27–36.
[5] E. Sher, G. Pinhasi, A. Pokryvailo, R. Bar-On, Extinction of pool flames by means of a DC electric field, Combustion and Flame 94 (1993) 244–252.
[6] D. L. Wisman, S. D. Marcum, B. N. Ganguly, Electrical control of the thermodiffusive instability in premixed propane-air flames, Combustion and Flame 151 (2007) 639–648.
[7] A. R. Hutchins, W. A. Reach, J. D. Kribs, K. M. Lyons, Effects of Electric Fields on Stabilized Lifted Propane Flames, Journal of Energy Resources Technology 136 (2014) 1–10.
[8] A. Cessou, E. Varea, K. Criner, G. Godard, P. Vervisch, Simultaneous measurements of OH, mixture fraction and velocity fields to investigate flame stabilization enhancement by electric field, Experiments in Fluids 52 (2012) 905–917.
[9] F. Altendorfner, F. Beyrau, A. Leipertz, T. Hammer, D. Most, G. Lins, D. W. Branston, Technical Feasibility of Electric Field Control for Turbulent Premixed Flames, Chemical Engineering & Technology 33 (2010) 647–653.
[10] F. Borgatelli, D. Dunn-Rankin, Behavior of a small diffusion flame as an electrically active component in a high-voltage circuit, Combustion and Flame 159 (2012) 210–220.
[11] N. Peters, Turbulent Combustion, Cambridge University Press, 2004.
[12] J. Urzay, Supersonic Combustion in Air-Breathing Propulsion Systems for Hypersonic Flight, Annual Review of Fluid Mechanics 50 (2018) 593–627.
[13] C. Guerra-Garcia, M. Martinez-Sanchez, Counterflow non-premixed flame DC displacement under AC electric field, Combustion and Flame 162 (2015) 4254–4263.
[14] S. K. Dayal, T. P. Pandya, Optical study of counterflow diffusion flames in transverse electric fields, Combustion and Flame 116 (1972) 113–116.
[15] S. K. Dayal, T. P. Pandya, Structure of counterflow diffustion flame in transverse electric fields, Combustion and Flame 35 (1979) 277–287.
[16] M. Belhi, B. J. Lee, F. Bisetti, H. G. Im, A computational study of the effects of DC electric fields on non-premixed counterflow methane-air flames, Journal of Physics D: Applied Physics 50 (2017) 494005.
[17] T. Pedersen, R. C. Brown, Simulation of electric field effects in premixed methane flames, Combustion and Flame 94 (1993) 433–448.
[18] F. Bisetti, M. El Morsli, Calculation and analysis of the mobility and diffusion coefficient of thermal electrons in methane/air premixed flames, Combustion and Flame 159 (2012) 3518–3521.
[19] N. Speelman, M. Kiefer, D. Markus, U. Maas, L. P. H. de Goey, J. A. van Oijen, Validation of a novel numerical model for the electric currents in burner-stabilized methaneair flames, Proceedings of the Combustion Institute 35 (2015) 847–854.
[20] J. Han, M. Belhi, F. Bisetti, Numerical modeling of ion transport in flames, Combustion Theory and Modelling 19 (2015) 744–772.
[21] Y. Xiong, D. G. Park, B. J. Lee, S. H. Chung, M. S. Cha, DC field response of one-dimensional flames using an ionized layer model, Combustion and Flame 163 (2016) 317–325.
[22] J. Prager, U. Riedel, J. Warnatz, Modeling ion chemistry and charged species diffusion in lean methane-oxygen flames, Proceedings of the Combustion Institute 31 (2007) 1129–1137.
[23] J. Hu, B. Rivin, E. Sher, The effect of an electric field on the shape of co-flowing and candle-type methaneair flames, Experimental Thermal and Fluid Science 21 (2000) 124–133.
[24] M. J. Papac, Effects of Electric Fields on Convection in Combustion Plasmas and Surrounding Gases, 36th AIAA Plasmadynamics and Lasers Conference (2005).
[25] K. Yamashita, S. Karnani, D. Dunn-Rankin, Numerical prediction of ion current from a small methane jet flame, Combustion and Flame 156 (2009) 1227–1233.
[26] M. Belhi, P. Domingo, P. Vervisch, Direct numerical simulation of the effect of an electric field on flame stability, Combustion and Flame 157 (2010) 2286–2297.
[27] M. Belhi, P. Domingo, P. Vervisch, Modelling of the effect of DC and AC electric fields on the stability of a lifted diffusion methane/air flame, Combustion Theory and Modelling 17 (2013) 749–787.
[28] M. Di Renzo, P. De Palma, M. D. de Tullio, G. Pascazio, An efficient flamelet progress-variable method for modeling non-premixed flames in weak electric fields, Computers & Fluids 157 (2017) 14–27.
[29] G. P. Smith, D. M. Golden, M. Frenklach, N. W. Moriarty, B. Eiteneer, M. Goldenberg, C. T. Bowman, R. K. Hanson, S. Song, W. C. J. Gardiner, V. V. Lissianski, Z. Qin, 2000, Grimech 3.0, URL: `http://www.me.berkeley.edu/gri_mech/`.
[30] N. Speelman, L. P. H. de Goey, J. A. van Oijen, Development of a numerical model for the electric current in burner-stabilised methaneair flames, Combustion Theory and Modelling 19 (2015) 159–187.
[31] H. Pitsch, 1998, Flamemaster v3.3.10: A c++ computer program for 0d combustion and 1d laminar flame calculations, URL: `http://www.itv.rwth-aachen.de/en/downloads/flamemaster/`.
[32] J. Han, M. Belhi, T. A. Casey, F. Bisetti, H. G. Im, J. Y. Chen, The i-V curve characteristics of burner-stabilized premixed flames: Detailed and reduced models, Proceedings of the Combustion Institute 36 (2017) 1241–1250.
[33] W. K. Metcalfe, S. M. Burke, S. S. Ahmed, H. J. Curran, A hierarchical and comparative kinetic modeling study of C1 - C2 hydrocarbon and oxygenated fuels, International Journal of Chemical Kinetics 45 (2013) 638–675.
[34] H. Wang, X. You, A. V. Joshi, S. G. Davis, A. Laskin, F. Egolfopoulos, C. K. Law, USC Mech Version II. High-Temperature Combustion Reaction Model of H2/CO/C1-C4 Compounds, 2007.
[35] K. Seshadri, N. Peters, Asymptotic structure and extinction of methane-air diffusion flames, Combustion and Flame 73 (1988) 23–44.
[36] H. Pitsch, N. Peters, A Consistent Flamelet Formulation for Non-Premixed Combustion Considering Differential Diffusion Effects, Combustion and Flame 114 (1998) 26–40.
[37] A. Liñán, The asymptotic structure of counterflow diffusion flames for large activation energies, Acta Astronautica 1 (1974) 1007–1039.
[38] D. Park, M. S. Cha, Private Communication, 2016.

The effects of incident electric fields on counterflow diffusion flames
Supplementary Material

Mario Di Renzo[a,b], Javier Urzay[a], Pietro De Palma[b], Marco D. de Tullio[b] and Giuseppe Pascazio[b]

[a] Center for Turbulence Research, Stanford University, Stanford, CA 94305-3024, United States
[b] Dipartimento di Meccanica, Matematica e Management & Centro di Eccellenza in Meccanica Computazionale, Politecnico di Bari, Bari 70125, Italy

S1. Formulation

In this section, the conservation equations and associated boundary conditions are provided. The description includes details of the calculation of transport properties and chemical rates, and outlines the numerical methodology employed in integrating the overall formulation.

S1.1. Conservation equations

The present analysis pertains to the obtention of steady laminar solutions of the conservation equations in the configuration depicted in Fig. 1 in the main text. As a result, the time derivatives are omitted in what follows. The resulting mass and momentum conservation equations are

$$\nabla \cdot \big(\rho \mathbf{u}\big) = 0, \tag{S1.1}$$

$$\nabla \cdot \big(\rho \mathbf{u}\mathbf{u}\big) = -\nabla p + \nabla \cdot \overline{\overline{\sigma}} + \mathbf{f}_{\mathbf{el}}, \tag{S1.2}$$

where ρ is the mixture density, $\mathbf{u}$ is the velocity vector, p is the hydrodynamic pressure, ∇ is the nabla operator in cylindrical coordinates, and $\mathbf{f}_{\mathbf{el}}$ is an electric force per unit volume that is defined below. Similarly, $\overline{\overline{\sigma}} = 2\eta[\overline{\overline{S}} - (\nabla \cdot \mathbf{u})\overline{\overline{\mathcal{I}}}/3]$ is the viscous stress tensor, where η is a temperature-dependent dynamic viscosity, $\overline{\overline{\mathcal{I}}}$ is the identity tensor, and $\overline{\overline{S}} = (1/2)[\nabla \mathbf{u} + (\nabla \mathbf{u})^T]$ is the strain-rate tensor.

The local mixture composition is obtained by integrating the species conservation equation

$$\nabla \cdot (\rho \mathbf{u} Y_i) = -\nabla \cdot (\rho \mathbf{V}_i Y_i) + \rho \dot{w}_i, \qquad i = 1, 2, \ldots, N_s, \tag{S1.3}$$

where N_s is the number of components, Y_i is the mass fraction of species i, and $\dot{w}_i$ and $\mathbf{V}_i$ are the corresponding chemical production rate and diffusion velocity, respectively. Specifically, $\dot{w}_i$ is computed from a detailed $CH_4/O_2/N_2$ chemical mechanism that includes ionic chemistry, as described in the main text in Sec. S1.2. Similarly, the diffusion velocity $\mathbf{V}_i$ is calculated from the expression

$$\mathbf{V}_i = -\frac{D_i}{X_i}\nabla X_i + \mu_i \mathcal{S}_i \mathbf{E} + \sum_{j=1}^{N_s}\left[\frac{Y_j}{X_j} D_j \nabla X_j - \mu_j \mathcal{S}_j Y_j \mathbf{E}\right], \tag{S1.4}$$

where X_i, D_i, and μ_i are, respectively, the molar fraction, mass diffusivity and electric mobility of species i. Additionally, $\mathcal{S}_i$ is the number of elementary charges in multiples of e, where $e = 1.602\,18 \times 10^{-19}$ C is the absolute value of the electron charge. In this way, $\mathcal{S}_i = 0$ for neutral species, and $\mathcal{S}_i > 0$ and $\mathcal{S}_i < 0$ for positively and negatively charged species, respectively.

The right-hand side of Eq. (S1.4) consists of three different terms: the first one represents the molecular diffusion flux in the Curtiss-Hirschfelder approximation [1]; the second one corresponds to a velocity drift of charged species that is induced by the local electric field $\mathbf{E}$ [2]; and the last term is a corrector flux that preserves the total mass of the multicomponent mixture [3]. In practice, the mass corrector for the electric drift is negligibly small compared to the other three terms, since the mass fractions of the ionic species involved in this analysis are of order $10^{-8} - 10^{-12}$.

The description of the chemically reacting flow requires additional integration of the energy conservation equation

$$\begin{aligned} c_p \nabla \cdot \big(\rho \mathbf{u} T\big) =& \nabla \cdot \big(\lambda \nabla T\big) - \rho \sum_{i=1}^{N_s} Y_i c_{p_i} \mathbf{V}_i \cdot \nabla T \\ & - \rho \sum_{i=1}^{N_s} h_i \dot{w}_i + \rho N_A e \sum_{i=1}^{N_s} \frac{\mathcal{S}_i Y_i}{W_i} \mathbf{V}_i \cdot \mathbf{E}, \end{aligned} \tag{S1.5}$$

where $c_p = \sum_{i=1}^{N_s} Y_i c_{p_i}$ is the mean specific heat at constant pressure, with c_{p_i} indicating the corresponding temperature-dependent value for species i. Additionally, $h_i = \int_{T_0}^{T} c_{p_i} dT$ is the partial specific enthalpy, W_i is the molecular weight of species i, N_A is the Avogadro number, and λ is a thermal conductivity that also depends on temperature, as detailed below. The right-hand side of Eq. (S1.5) includes, in order of appearance, the molecular heat conduction, a heat flux due to inter-diffusion of species, the heat released by the chemical reactions, and the Ohmic dissipation of energy due to electric currents. The viscous heating and the work done by the pressure gradient are both neglected because of the low Mach numbers involved.

The DC voltage applied on the electrodes generates an incident electric field $\mathbf{E}$ that is coupled with the charged

reaction intermediates in the diffusion flame. The nature of the local electric field is electrostatic, and is therefore derived from a local potential Φ as

$$\mathbf{E} = -\nabla\Phi, \tag{S1.6}$$

where Φ is the solution to the Gauss equation

$$\nabla^2\Phi = -\rho_q/\epsilon_0, \tag{S1.7}$$

with ϵ_0 as the permittivity of vacuum. In this formulation, $\rho_q = \sum_{i=1}^{N_s} \rho_{q,i}$ denotes the sum of the individual charge densities

$$\rho_{q,i} = \rho N_A e \frac{\mathcal{S}_i Y_i}{W_i}. \tag{S1.8}$$

representing the amount of charge carried by species i per unit volume. In the present calculations, the magnetic field induced by the Ampere's law is of order 10^{-9} T, and is therefore neglected on the basis of the resulting exceedingly long cyclotron period. Correspondingly, the Lorentz force per unit volume is solely associated with the electric field and is given by

$$\mathbf{f_{el}} = \rho_q \mathbf{E} = \rho N_A e \sum_{i=1}^{N_s} \frac{\mathcal{S}_i Y_i}{W_i} \mathbf{E}. \tag{S1.9}$$

Equations (S1.1)-(S1.9) are supplemented with the equation of state for an ideal gas

$$P = \rho \mathrm{R}^0 T/\overline{W}, \tag{S1.10}$$

where $\overline{W} = (\sum_{i=1}^{N_s} Y_i/W_i)^{-1}$ is the mean molecular weight, R^0 is the universal gas constant, and P is the thermodynamic pressure, which is assumed to be uniform in the present low-Mach number approximation. In the conservation equations described above, the temperature is assumed to be the same for neutrals, ions and electrons, thus neglecting non-thermalization effects, as is appropriate for the moderate reduced electric fields $|\mathbf{E}|\overline{W}/(\rho N_A) \sim 10-70$ Td encountered in the present study [4].

S1.2. Chemical kinetics

In this study, the chemical reaction rates for the combustion of methane with oxygen in nitrogen-diluted environments are calculated using the GRIMech 3.0 mechanism [5], which contains 325 reactions among 53 neutral species. The mechanism is augmented with the reactions proposed by Belhi *et al.* [6] to model the chemical conversion of ionized species. This additional submechanism consists of 40 reversible reactions involving H_3O^+, CHO^+, $O_2{}^-$, O^-, OH^-, and e^-. A brief summary of the main reactions involving ionized species is provided below.

Of particular relevance in this chemical-kinetic description is the chemi-ionization reaction

$$\mathrm{CH + O \longrightarrow CHO^+ + e^-}, \tag{R1}$$

which represents the only ionization step of the mechanism, whereby the two intermediates CH and O are transformed into formylium (CHO^+) and electrons (e^-). The formylium produced by step (R1) is rapidly transformed into hydronium (H_3O^+) through the charge-transfer reaction

$$\mathrm{CHO^+ + H_2O \longrightarrow H_3O^+ + CO}, \tag{R2}$$

as suggested by Pedersen and Brown [2]. A portion of the electrons produced in the flame react in 13 three-body electron-attachment reactions to produce $O_2{}^-$, O^- and OH^- from neutral molecules. This set of reactions can be summarized in the following steps

$$\mathrm{O_2 + e^- + M \longrightarrow O_2{}^- + M}, \tag{R3}$$

$$\mathrm{OH + e^- + M \longrightarrow OH^- + M}, \tag{R4}$$

$$\mathrm{O + e^- + M \longrightarrow O^- + M}, \tag{R5}$$

where M is a collider (i.e., M = O, O_2, H_2O, and N_2 for R3; M = H_2, O_2, H_2O, N_2, CO, CO_2, and CH_4 for R4; and M = O_2 and O for R5). Two charge-exchange reactions

$$\mathrm{O_2{}^- + O \longrightarrow O_2 + O^-} \tag{R6}$$

$$\mathrm{O_2{}^- + OH \longrightarrow O_2 + OH^-} \tag{R7}$$

are included that account for extra formation of O^- and OH^- [7]. In addition, 6 charge-transfer reactions with rearrangement, where the $O_2{}^-$ and O^- interact with a neutral molecule, are responsible for the formation of charged particles that correspond to the combination of the two reactants, while 16 electron-detachment reactions release electrons from heavy molecules. Lastly, the electrons are recombined with the hydronium through the dissociative recombination reaction

$$\mathrm{H_3O^+ + e^- \longrightarrow H_2O + H}, \tag{R8}$$

which represents, as also done in earlier studies [2, 8, 9], the termination reaction of this submechanism for ionic chemistry. The reaction parameters of the recombination step (R8) are chosen to match the global recombination rate measured by Peeters and Mahnen [10].

The choice of chemical kinetics made above represents a compromise solution between accuracy and computational cost. As suggested by the results presented in this study, this choice is most likely not the optimum one in terms of accuracy, since other more extensive mechanisms such as the ones in Refs. [11, 12] might improve the predictions of the CH and O radicals and consequently assist in reducing the discrepancies observed in the saturation current with respect to experimental results (i.e., see Sec. 3.1 in the main text and Sec. S2 below for further details). Those extended mechanisms would, however, incur a computational cost that is not easily admissible with the present numerical method because of the large number of additional species that would need to be transported.

S1.3. Transport coefficients

The individual dynamic viscosities (η_i) and binary diffusivities (D_{ij}) are evaluated from the kinetic theory as in Hirschfelder *et al.* [13], namely

$$\eta_i = \frac{5}{16}\frac{\sqrt{\pi k_B T W_i/N_A}}{\pi\sigma_i^2\Omega_i^{(2,2)}} \tag{S1.11}$$

and

$$D_{ij} = \frac{3}{16}\frac{\sqrt{2\pi N_A k_B^3 T^3/W_{ij}}}{p\pi\sigma_{ij}^2\Omega_{ij}^{(1,1)}}, \tag{S1.12}$$

where k_B is the Boltzmann constant, σ_i is the Lennard-Jones collision diameter, $\sigma_{ij} = (\sigma_i + \sigma_j)/2$ is the reduced collision diameter, and $W_{ij} = W_i W_j/(W_i + W_j)$ is the reduced molecular weight. Additionally, $\Omega_{ij}^{(1,1)}$ and $\Omega_i^{(2,2)}$ are collision integrals that are expressed as polynomials of the reduced temperature $T_i^* = Tk_B/\xi_i$ (for $\Omega_i^{(2,2)}$) and $T_{ij}^* = Tk_B/\sqrt{\xi_i\xi_j}$ (for $\Omega_{ij}^{(1,1)}$), where ξ_i is the potential well-depth of species i. In this study, the Stockmayer potential [14] is employed to calculate the temperature coefficients of the collision integrals $\Omega_{ij}^{(1,1)}$ and $\Omega_i^{(2,2)}$ for neutrals and heavy ions. For the neutral species, σ_i and ξ_i are read from the transport data provided with the GriMech 3.0 mechanism [5]. On the other hand, the corresponding values for the heavy ions are approximated to be equal to those of similar neutral species (i.e., H_2O for H_3O^+, CO for HCO^+, O for O^-, O_2 for $O_2{}^-$ and OH for OH^-). Other alternatives, such as the (n, 6, 4) theory [15], may be more appropriate for the prediction of the transport properties of the charged species, but those involve additional complexities and modeling uncertainties whose treatment are deferred to future work.

The individual thermal conductivities are computed using the expression

$$\lambda_i = \eta_i\left(c_{p_i} + \frac{5}{4}\frac{\mathrm{R}^0}{W_i}\right) \tag{S1.13}$$

resulting from the kinetic-theory for monoatomic gases, with η_i given by Eq. (S1.11). The temperature dependence of the individual specific heats c_{p_i} are modeled using the NASA polynomials [16]. The polynomial coefficients for the neutrals species are provided by the GriMech 3.0 mechanism [5], while those for the charged species are extracted from the database of Burcat and Ruscic [17].

The mass diffusivities of each component into the other components of the mixture are evaluated using the approximate expression

$$D_i = (1 - Y_i)\Bigg/\sum_{j=1, j\neq i}^{N_s}\frac{X_j}{D_{ij}} \tag{S1.14}$$

proposed by Bird *et al.* [18], with D_{ij} given by Eq. (S1.12). Combination rules are followed to calculate the thermal conductivity λ and dynamic viscosity η of the mixture in terms of the corresponding individual quantities η_i and λ_i defined in Eqs. (S1.11) and (S1.13), respectively. In particular, η is determined using Wilke's rule [19]

$$\eta = \left(\sum_{i=1}^{N_s} Y_i\eta_i\right)\Bigg/\left(\sum_{j=1}^{N_s} G_{ij}\frac{W_i}{W_j}Y_j\right), \tag{S1.15}$$

where the symbol G_{ij} is given by

$$G_{ij} = \frac{1}{\sqrt{8}}\left(1 + \frac{W_i}{W_j}\right)^{-\frac{1}{2}}\left[1 + \left(\frac{\eta_i}{\eta_j}\right)^{-\frac{1}{2}}\left(\frac{W_j}{W_i}\right)^{\frac{1}{4}}\right]^2. \tag{S1.16}$$

Similarly, λ is computed from Ref. [20], namely

$$\lambda = \frac{1}{2}\left[\sum_{i=1}^{N_s} X_i\lambda_i + \left(\sum_{i=1}^{N_s}\frac{X_i}{\lambda_i}\right)^{-1}\right]. \tag{S1.17}$$

The binary mobilities of the heavy ions, μ_{ij} are obtained from the Einstein relation [21]

$$\frac{D_{ij}}{\mu_{ij}} = \frac{k_B T}{e}, \tag{S1.18}$$

while the corresponding mixture-averaged value μ_i is computed using the expression [21]

$$\mu_i = \left(\sum_{j=1}^{N_s}\frac{X_j}{\mu_{ij}}\right)^{-1}. \tag{S1.19}$$

An important role in the calculations shown in Sec. 3 is played by the mobility of electrons μ_{e^-}, since its value determines the rate at which the electrons are drained from the flame in the sub-saturated regime, and also influences the voltage and the amount of ion current measured at the electrodes at the saturation onset [22]. It should however be noted that the analytical and experimental determination of adequate mobility coefficients for diffusion flames is an active area of research. In this study, in the absence of conclusive values for diffusion flames, the electron mobility μ_{e^-} is set to $0.4\,\mathrm{m}^2/(\mathrm{s\,V})$ as recommended by Bisetti and El Morsli [4, 23] in the context of premixed CH_4-air flames. Note that more elaborate formulations of the electron mobility exist that provide spatially varying distributions of this quantity depending on the local composition [23].

The value of the electron mobility has an important influence on the simulation cost, in that the larger μ_{e^-} is, the shorter is the electric drift diffusion time scale of the electrons, and consequently, the stiffer the numerical integrations become. In this regard, the value of μ_{e^-} considered here is much larger than that used in earlier numerical studies [6, 24, 25] and based on the scaling proposed by Delcroix and Bers [26] [i.e., $\mu_{e^-} \sim 0.018\,\mathrm{m}^2/(\mathrm{s\,V})$]. This illustrates the large uncertainties associated with the values of μ_{e^-} that exist in the available literature. Consistently with this choice, the electron mass diffusivity D_{e^-} is computed from the standard Einstein mobility expression

$$D_{e^-} = \frac{k_B\mu_{e^-}T}{e}. \tag{S1.20}$$

S1.4. Numerical method

The conservation equations provided above are integrated using a numerical method that consists of an extended version of the finite-difference fractional-step method described by Desjardins *et al.* [27], which has been employed in a number of earlier studies to compute chemically reacting flows [28–30]. The present study incorporates modifications to address electric interactions in combustion problems and to palliate the significant numerical stiffness caused by the ionic chemistry and electron transport as follows.

Motivated by the moderate Reynolds numbers associated with this configuration, this study aims at obtaining steady solutions to the conservation equations. However, although there is yet no clear general criteria available about the voltage conditions under which flow unsteadiness may develop as a result of electrically-induced combustion instabilities, the experiments of Park *et al.* [31] suggest the existence of flame oscillations within a narrow interval of voltages near saturation conditions (i.e., $|\Delta\Phi_0| \sim 1.1 - 1.3$kV for the case $Z_{st} = 0.50$), while steady conditions are observed for all other tested voltages. In this context, time-resolved simulations of unsteady behavior are challenging due to the small time steps of order $\Delta t = L\Delta x/(\mu_{e^-}|\Delta\Phi_0|) = \mathrm{O}(0.1\,\mathrm{ns})$ that would be required to advance the transport equation for the electrons, which, when compared to the characteristic flow times $A^{-1} \sim 2L/U = \mathrm{O}(10\,\mathrm{ms})$ under consideration, would result in an unfeasible large number of simulation steps of order 10^8. For these reasons, and since the experimental voltage interval reported as prone to triggering flame instabilities is not directly probed by these simulations, in the present formulation unsteady effects are neglected, and each conservation equation is discretely advanced using a pseudo-time increment in order to efficiently arrive at a steady-state solution. The pseudo-time stepping algorithm adds an extra derivative with respect to a pseudo-time τ in the conservation equations (S1.1)-(S1.3) and (S1.5), each equation having its own pseudo-time step due to inherent limitations related to the participating time scales.

In addition to the fast transport of electrons, exceedingly short time scales of chemical conversion are also found within the set of reactions involving charged species. This also contributes to the stiffness of the employed system of partial differential equations requiring a special implicit treatment of the evolution of the chemical sources terms. For these reasons, the conservation equations for species (S1.3) and thermal energy (S1.5) are cast into the ordinary differential forms

$$\frac{d}{d\tau}[Y_i, T] = \frac{\nabla \cdot F^0}{\rho^0} + \left[\dot{w}_i, \frac{\dot{w}_T}{c_p}\right], \tag{S1.21}$$

for $i = 1, \ldots, N_s$, where $\dot{w}_T = -\sum_{i=1}^{N_s} h_i \dot{w}_i$ is the chemical heat release. In Eq. (S1.21), F^0 represents advective and diffusive fluxes based on the solution of the previous pseudo-time step, ρ^0 is the mixture density computed at the previous pseudo-time step, while the chemical sources ($\dot{w}_i$, $\dot{w}_T$) and c_p are evaluated implicitly. These equations are solved point-wise and coupled between all variables using a Newton-based implicit method over a pseudo-time interval determined as the maximum value among the pseudo-time step of the temperature ($\Delta\tau_T$) and of all the species mass fraction equations ($\Delta\tau_i$), $\Delta\tau = \max(\Delta\tau_T, \Delta\tau_1, \ldots, \Delta\tau_{N_s})$. In particular, the pseudo-time step for the transport of thermal energy is chosen as $\Delta\tau_T = \min(\Delta x/|u_x|, \Delta r/|u_r|)$, whereas the corresponding value for the species transport is set to $\Delta\tau_i = \min(\Delta x/|u_x + \mathcal{S}_i\mu_i E_x|, \Delta r/|u_r + \mathcal{S}_i\mu_i E_r|)$, where the subindexes $_x$ and $_r$ are employed to denote velocity and electric-field components in the axial and radial directions, respectively. Note that the $\Delta\tau_i$ for the neutral species ($\mathcal{S}_i = 0$) is equal to $\Delta\tau_T$ because their electric drift velocities vanish. In this way, the intermediate solutions $Y_i(\tau + \Delta\tau)$ and $T(\tau + \Delta\tau)$ emerging from the numerical integration of (S1.21) only account for the time evolution of the chemistry over the longest interval $\Delta\tau$ among all the different pseudo-time steps. These intermediate solutions are stored during the integration and are employed to define the species averaged chemical source terms

$$\overline{\dot{w}_i} = \frac{Y_i(\tau + \Delta\tau_i) - Y_i(\tau)}{\Delta\tau_i} - \frac{\nabla \cdot F^0}{\rho^0}, \tag{S1.22}$$

with $\overline{\dot{w}_i} = \dot{w}_i$ being satisfied in the steady state. The averaged chemical heat release per mass unit is then computed as $\overline{\dot{w}_T} = \sum_{i=1}^{N_s} h_i \overline{\dot{w}_i}$. The resulting computational cost of the implicit integration described above scales as N_s^2.

The algorithm of the numerical integration of the problem is structured as follows. Once the averaged chemical source terms are obtained by the procedure described above, and after computing transport properties based on the most recent solution of the species and temperature transport equations, the conservation equations (S1.3) - (S1.5) for the neutral species and thermal energy are advanced over the corresponding pseudo-time steps $\Delta\tau_i$ and $\Delta\tau_T$ incorporating the effects of the advection and diffusion fluxes, for which the semi-implicit formulation in Desjardins *et al.* [27] is used. The advection fluxes in the species and thermal-energy conservation equations are discretized with a third-order weighted essentially-non-oscillatory scheme. The rest of the differential terms are computed using a second-order centered scheme. The linear system derived from the discretization of transport equations is solved using an alternate-direction algorithm.

A subiterative loop is then performed to solve the Poisson equation for the electrostatic potential in conjunction with the species transport equation for the charged particles (integrated over the corresponding pseudo-time steps $\Delta\tau_i$) to ensure consistency of the electric field with the electric charge. Note that the disparity in pseudo-time steps between the charged and neutral species acts as a diagonal preconditioning in the integration, with the ratio of the advection to drift velocities as the approximate values of the diagonal elements. At this point, the newly

computed species mass-fractions and temperature fields are used to update the local mixture density field from the equation of state (S1.10).

Lastly, the momentum conservation equation is time advanced using the pseudo-time step $\Delta\tau_T$ (i.e., limited by the flow velocity) in conjunction with the solution to the Poisson equation for the hydrodynamic pressure. Both Poisson equations for the hydrodynamic pressure and electrostatic potential are solved using a multi-grid preconditioned GMRES method. The algorithm steps covering from the advancement of the neutral species mass-fractions fields to the hydrodynamic pressure are repeated up to 10 times at each corresponding pseudo-time step in order to converge the density and keep the numerical method stable. Tests of the numerical methodology described above are provided in Sec. S2.

S2. Supplementary tests of the computational framework in simulations and experiments of burner-stabilized premixed flames

To address the performance of the computational approach presented in Sec. S1, additional numerical simulation results are reported below for a reference case consisting of burner-stabilized premixed flames, which has been treated both numerically and experimentally by Speelman *et al.* [22]. The analysis also includes successful comparisons with results obtained for the same problem using the Flamemaster code [32].

The configuration involves a burner-stabilized premixed flame immersed in an electric field that is aligned with the flow direction. In the experiments [22], a cylindrical nozzle of diameter 6 cm injects a stoichiometric mixture of CH_4 and air at at 298 K with a velocity equal to the laminar burning velocity of the mixture into an environment at atmospheric pressure. The exit of the burner is kept at a temperature of 350 K in order to stabilize the flame. One electrode is positioned at the exit of the nozzle, while the other is located at 1 cm downstream. A DC voltage ranging from -250 V to 250 V is applied to the downstream electrode, whereas the upstream one is kept grounded.

The formulation of the problem follows the same principles and relations described in Sec. S1. The computational set-up includes a one-dimensional (1D) grid discretizing the region between the two electrodes by means of 800 evenly spaced points. At the upstream boundary, Dirichlet boundary conditions are imposed for the velocity, neutral species, temperature and electric field. In particular, the temperature at that boundary is set equal to the burner temperature in order to generate the necessary heat loss to stabilizes the premixed flame near the injector. Similarly, the downstream boundary is modeled with a convective outflow condition for the aerothermal variables and for the mass fractions of the neutral species. The applied electric potential difference is translated into Dirichlet conditions at the upstream and downstream boundaries. The boundary conditions for the charged-species are analogous

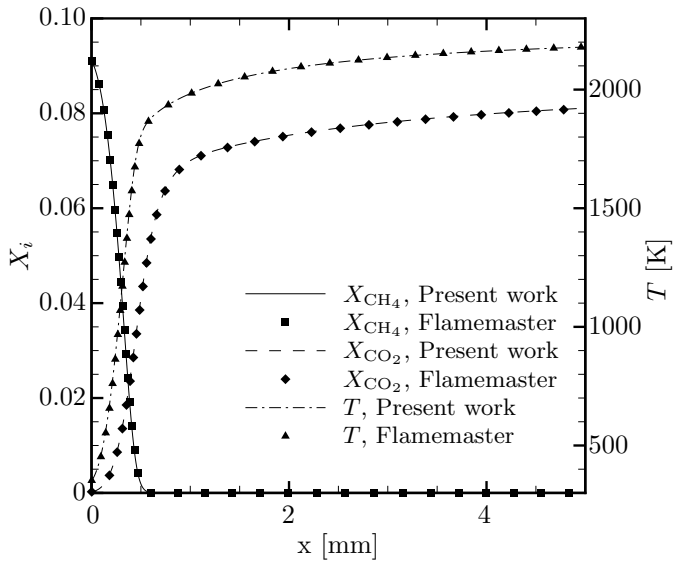

Figure S2.1: Spatial distributions of temperature and molar fractions of CH_4 and CO_2 through the flame. Symbols represent the solution obtained with Flamemaster, while lines correspond to results obtained with the present computational framework.

to those described in Sec. 2. Further details of the configuration are available in Ref. [22].

In addition to simulations of the aforementioned problem performed with the present approach, the code Flamemaster [32] was employed to verify the numerical method described in Sec. S1.4. In particular, the Flamemaster module for burner-stabilized 1D premixed flames, which employs different numerics (i.e., a Newton method, see details in Ref. [32]) than the present approach, was modified by adding to the original algorithm the Gauss equation (S1.7), the electric-drift terms in the diffusion velocity (S1.4), and the Ohmic dissipation term in the energy conservation equation (S1.5). Results of the numerical simulations of the configuration in Speelman *et al.* [22], subject to the same boundary conditions as described above and supplied with the same chemical mechanism and transport properties as those provided in Secs. S1.2 and S1.3, are shown in Fig. S2.1. The Flamemaster profiles of temperature and molar fractions of CH_4 and CO_2 across the flame are observed to agree well with the profiles obtained using the present computational framework.

Figure S2.2 shows the electric intensity (I) versus the voltage difference applied to the electrodes. The dash-dotted line represents the results obtained using the present computational approach, while the symbols correspond to solutions of the same problem obtained with Flamemaster, as described above, thereby showing a good agreement between the two. Additionally, the continuous line represents the experimental values provided by Speelman *et al.* [22]. The dashed line is, instead, obtained numerically also in Ref. [22] employing the chemical mechanism proposed by Belhi *et al.* [24] and a transport model based

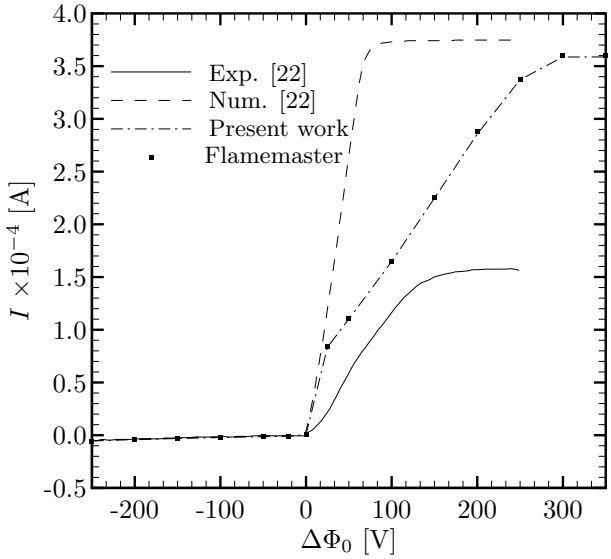

Figure S2.2: Electric intensity I as a function of the applied potential $\Delta\Phi_0$. The three curves represent the experiments and numerical results of Speelman *et al.* [22], along with the present study. Symbols represent the solution obtained with Flamemaster.

on the Stockmayer potentials in conjunction with the procedure proposed by Ern and Giovangigli [33]. Note that these numerical results in Speelman *et al.* [22] were computed without any case-specific optimization of the chemical mechanism and transport coefficients. However, in that same work, additional results were provided that showed an improved agreement with experiments, and which were obtained by tuning the electron and hydronium electrical mobilities along with the Arrhenius pre-exponential factors of the ionization and recombination reaction rates. In some cases, those revisions led to a sudden turn of the curve at $\Delta\Phi_0 \sim 20$ V similar to the one observed in the present results [22]. All curves in Fig. S2.2 remain monotonic since the coupling between the electric and hydrodynamic fields in this problem are weaker, in that the interaction mainly involves a readjustment of the hydrodynamic pressure without any significant feedback on the aerothermal field of the bulk gas.

Both numerical solutions presented in Fig. S2.2 predict a much larger saturation intensity than the experimentally measured one, although the present framework palliates the discrepancy by falling closer to the experiments. The discrepancy here is similar to the overprediction by a 2.5 factor reported for the counterflow diffusion flame in Sec. 3.1 in the main text. An additional aspect implied by Fig. S2.2 is that the present transport formulation and the introduction of heavy anions in the chemical description appears to largely improve predictions for the sub-saturated regime. Specifically, the present solution has a lower slope for the entire range of applied voltages, reaching the saturation current between 250 V and 300 V.

References

[1] C. F. Curtiss, J. O. Hirschfelder, Transport Properties of Multicomponent Gas Mixtures, The Journal of Chemical Physics 17 (1949) 550–555.

[2] T. Pedersen, R. C. Brown, Simulation of electric field effects in premixed methane flames, Combustion and Flame 94 (1993) 433–448.

[3] T. P. Coffee, J. M. Heimerl, Transport algorithms for premixed, laminar steady-state flames, Combustion and Flame 43 (1981) 273–289.

[4] F. Bisetti, M. El Morsli, Kinetic parameters, collision rates, energy exchanges and transport coefficients of non-thermal electrons in premixed flames at sub-breakdown electric field strengths, Combustion Theory and Modelling 18 (2014) 1–37.

[5] G. P. Smith, D. M. Golden, M. Frenklach, N. W. Moriarty, B. Eiteneer, M. Goldenberg, C. T. Bowman, R. K. Hanson, S. Song, W. C. J. Gardiner, V. V. Lissianski, Z. Qin, 2000, Grimech 3.0, URL: `http://www.me.berkeley.edu/gri_mech/`.

[6] M. Belhi, P. Domingo, P. Vervisch, Modelling of the effect of DC and AC electric fields on the stability of a lifted diffusion methane/air flame, Combustion Theory and Modelling 17 (2013) 749–787.

[7] J. M. Goodings, D. K. Bohme, Chun-Wai NG, Detailed ion chemistry in methane-oxygen flames. II. Negative ions, Combustion and Flame 36 (1979) 45–62.

[8] J. Hu, B. Rivin, E. Sher, The effect of an electric field on the shape of co-flowing and candle-type methaneair flames, Experimental Thermal and Fluid Science 21 (2000) 124–133.

[9] K. Yamashita, S. Karnani, D. Dunn-Rankin, Numerical prediction of ion current from a small methane jet flame, Combustion and Flame 156 (2009) 1227–1233.

[10] J. Peeters, G. Mahnen, Reaction Mechanisms and Rate Constants of Elementary Steps in Methane - Oxygen Flames, Symposium (International) on Combustion (1973).

[11] H. Wang, X. You, A. V. Joshi, S. G. Davis, A. Laskin, F. Egolfopoulos, C. K. Law, USC Mech Version II. High-Temperature Combustion Reaction Model of H2/CO/C1-C4 Compounds, 2007.

[12] W. K. Metcalfe, S. M. Burke, S. S. Ahmed, H. J. Curran, A hierarchical and comparative kinetic modeling study of C1 - C2 hydrocarbon and oxygenated fuels, International Journal of Chemical Kinetics 45 (2013) 638–675.

[13] J. O. Hirschfelder, C. F. Curtiss, R. B. Bird, Molecular theory of gases and liquids, John Wiley & Sons, 1964.

[14] L. Monchick, E. A. Mason, Transport Properties of Polar Gases, The Journal of Chemical Physics 35 (1961) 1676–1697.

[15] J. Han, M. Belhi, F. Bisetti, Numerical modeling of ion transport in flames, Combustion Theory and Modelling 19 (2015) 744–772.

[16] B. Mcbride, S. Gordon, M. Reno, Coefficients for Calculating Thermodynamic and Transport Properties of Individual Species, Nasa Technical Memorandum 4513 (1993) 98.

[17] A. Burcat, B. Ruscic, 2005, Third millennium ideal gas and condensed phase thermochemical database for combustion with updates from active thermochemical tables, URL: `http://garfield.chem.elte.hu/Burcat/burcat.html`.

[18] R. B. Bird, W. E. Stewart, E. N. Lightfoot, Transport phenomena, John Wiley & Sons, Inc., New York, 1960.

[19] C. R. Wilke, A Viscosity Equation for Gas Mixtures, The Journal of Chemical Physics 18 (1950) 517–519.

[20] S. Mathur, P. K. Tondon, S. C. Saxena, Molecular Physics Thermal conductivity of binary, ternary and quaternary mixtures of rare gases Thermal conductivity of binary, ternary and quaternary mixtures of rare gases, Molecular Physics 12 (1967) 569–579.

[21] E. A. Mason, E. W. McDaniel, Transport Properties of Ions in Gases, Wiley, New York, 1988.

[22] N. Speelman, L. P. H. de Goey, J. A. van Oijen, Development of a numerical model for the electric current in burner-stabilised methaneair flames, Combustion Theory and Modelling 19 (2015) 159–187.

[23] F. Bisetti, M. El Morsli, Calculation and analysis of the mobility and diffusion coefficient of thermal electrons in methane/air premixed flames, Combustion and Flame 159 (2012) 3518–3521.
[24] M. Belhi, P. Domingo, P. Vervisch, Direct numerical simulation of the effect of an electric field on flame stability, Combustion and Flame 157 (2010) 2286–2297.
[25] M. Di Renzo, P. De Palma, M. D. de Tullio, G. Pascazio, An efficient flamelet progress-variable method for modeling non-premixed flames in weak electric fields, Computers & Fluids 157 (2017) 14–27.
[26] J.-L. Delcroix, A. Bers, Physique del Plasmas, Vol. 2, EDP Sciences, 1994.
[27] O. Desjardins, G. Blanquart, G. Balarac, H. Pitsch, High order conservative finite difference scheme for variable density low Mach number turbulent flows, Journal of Computational Physics 227 (2008) 7125–7159.
[28] V. Mittal, H. Pitsch, F. Egolfopoulos, Assessment of counterflow to measure laminar burning velocities using direct numerical simulations, Combustion Theory and Modelling 16 (2012) 419–433.
[29] E. Knudsen, H. Pitsch, A general flamelet transformation useful for distinguishing between premixed and non-premixed modes of combustion, Combustion and Flame 156 (2009) 678–696.
[30] M. E. Mueller, G. Iaccarino, H. Pitsch, Chemical kinetic uncertainty quantification for Large Eddy Simulation of turbulent nonpremixed combustion, Proceedings of the Combustion Institute (2012) 1–16.
[31] D. G. Park, S. H. Chung, M. S. Cha, Bidirectional ionic wind in nonpremixed counterflow flames with DC electric fields, Combustion and Flame 168 (2016) 138–146.
[32] H. Pitsch, 1998, Flamemaster v3.3.10: A c++ computer program for 0d combustion and 1d laminar flame calculations, URL: `http://www.itv.rwth-aachen.de/en/downloads/flamemaster/`.
[33] A. Ern, V. Giovangigli, Multicomponent transport algorithms, volume 24 of *Lecture Notes in Physics Monographs*, Springer Berlin Heidelberg, Berlin, Heidelberg, 1994.